HHS Public Access

Author manuscript

Nat Neurosci. Author manuscript; available in PMC 2018 July 22.

Published in final edited form as:

Nat Neurosci. 2018 February ; 21(2): 218–227. doi:10.1038/s41593-017-0064-2.

Inhibitory circuit gating of auditory critical period plasticity

Anne E. Takesian[1,2], **Luke J. Bogart**[2], **Jeff W. Lichtman**[2], and **Takao K. Hensch**[1,2]

[1]FM Kirby Neurobiology Center, Boston Children's Hospital, Boston, Massachusetts, USA

[2]Center for Brain Science, Department of Molecular & Cellular Biology, Harvard University, Cambridge, Massachusetts, USA

SUMMARY

Cortical sensory maps are remodeled during early life to adapt to the surrounding environment. Both sensory and contextual signals play an important role, but how these two inputs converge to sculpt developing thalamocortical circuits remains largely unknown. Here, we reveal layer 1 (L1) of primary auditory cortex (A1) to be a key hub where neuromodulatory and topographically-organized thalamic inputs meet to tune the cortical layers below. Inhibitory interneurons in L1 send narrowly descending projections to differentially modulate thalamic drive onto pyramidal and parvalbumin-expressing (PV) cells in L4, creating brief windows of intracolumnar activation. Silencing L1 (but not VIP) cells abolishes map plasticity during the tonotopic critical period. Instead, developmental transitions of nicotinic acetylcholine receptor (nAChR) sensitivity in these cells by the Lynx1 protein can be overridden to extend critical period closure. Notably, thalamocortical maps in L1 are themselves stable, serving as a scaffold for cortical plasticity throughout life.

Keywords

5HT3; GABA; tonotopy; brainbow; nicotinic; Lynx1

MAIN TEXT

Our individualized perception of the external world is established during windows of early life when sensory circuits adapt to the surrounding environment. During such 'critical periods', infants for example become rapidly attuned to relevant speech sounds heard repeatedly[1,2]. Perceptual narrowing may occur in part by a restructuring of sound frequency maps (tonotopy) in the developing auditory cortex[3–5]. How experience sculpts sensory maps, and why this robust plasticity is restricted to early life remains poorly understood.

Correspondence should be addressed to Takao K. Hensch (hensch@mcb.harvard.edu).

AUTHOR CONTRIBUTIONS

A.E.T. and T.K.H. designed the study and wrote the manuscript. A.E.T. conducted the experiments, and analyzed the data. J.W.L. and L.J.B. assisted with the Brainbow experiments, imaging and analysis.

COMPETING FINANCIAL INTERESTS

The authors declare no competing financial interests.

Identifying neural targets defining these windows of cortical plasticity would offer both novel insight into neurodevelopmental disorders and potential strategies to promote plasticity in adulthood.

A convergence of sensory and contextual signals is thought to underlie the refinement of functional connectivity within the developing brain[6]. Where such signals meet to drive plasticity within thalamocortical circuits is unclear. Located directly beneath the pial surface, cortical L1 may be one such site, integrating diverse projections[7–9] including neuromodulatory axons that target the sparse cells there[10,11]. Nearly all L1 neurons bear ionotropic 5-HT_{3A}R receptors, a unique marker for one of three major sub-populations of cortical inhibitory interneurons[10]. Perhaps by punching "holes" within networks of blanket inhibition[12], 5-HT_{3A}R cells are emerging as important controllers of adult cortical activity by targeting other GABAergic cells[12–17]. However, the impact of L1 cells in the developing brain remains unknown.

Here, we reveal 5-HT_{3A}R cells to be key sites of convergence for sensory and neuromodulatory inputs to orchestrate critical period plasticity in the primary auditory cortex (A1). Moreover, these cells form an unexpected topographic map that is engaged early in life by transiently enhanced nicotinic acetylcholine receptor (nAChR) function, serving as a scaffold to gate plasticity in the cortical layers below.

RESULTS

Neuromodulatory and sensory signals converge upon superficial 5-HT_{3A}R interneurons

The canonical model of A1 circuitry dictates that input from the primary auditory thalamus, the ventral medial geniculate body (MGB), terminates within cortical L4. However, several reports suggest that divisions of MGB also send projections to L1[18–20]. Expressing an anterograde viral tracer in MGB cells to visualize their projections to A1, we found a robust innervation of cortical L1 (Fig. 1a,b). MGB axons surrounded L1 interneurons, forming putative contacts that co-localized with the vesicular glutamate transporter 2 (vGluT2), a marker of thalamocortical boutons[21] (Supplementary Fig. 1).

Upon electrical stimulation of MGB fibers in auditory thalamocortical slices, the average minimum and maximum amplitudes of excitatory postsynaptic potentials (EPSPs) in L1 interneurons were similar in strength to those recorded in L4 pyramidal cells (Fig. 1c–e). Both L1 interneuron subtypes that fire either non-adapting, late-spiking action potentials (LS) or adapting, non-late-spiking action potentials[14] (non-LS), showed comparable EPSP amplitudes (Supplementary Fig. 2a,b).

A low average coefficient of variation (CV) of the EPSP onset rise time was seen in both L1 and L4 pyramidal cells, further consistent with a monosynaptic connection from the MGB[22] (Fig. 1e). Despite slower EPSP onset latency in L1 interneurons reflecting axonal conduction delay from L4 to L1**,** MGB-evoked EPSPs in both layers displayed similar rise times and half-widths (Supplementary Fig. 2a,b). Finally, the EPSPs recorded during trains of MGB stimuli in L1 interneurons exhibited short-term depression as in L4 cells

(Supplementary Fig. 2c,d). Together, these results provide evidence for a strong, temporally-precise MGB connection to L1 interneurons within A1.

Notably, L1 is also a target of neuromodulatory inputs, such as cholinergic axons[10,11] (Fig. 1f). 5-HT_{3A}R interneurons exhibited EPSPs by focal application of both the selective 5-HT_3R agonist, m-CPBG and the nAChR-selective agonist, nicotine (100μM; Fig. 1g). Using fluorescence-activated cell sorting (FACS) to examine gene expression in the three subpopulations of interneurons — parvalbumin- (PV), somatostatin- and 5-HT_{3A}R-expressing cells[10] — we found the genes encoding the major nAChR subunits (α7, α4, and β2) to be expressed preferentially in 5-HT_{3A}R interneurons (Fig. 1h). Therefore, L1 interneurons are direct sites of convergence for sensory inputs from the MGB and fast neuromodulatory inputs.

Narrowly descending 5HT_{3A}R cell axons target intracolumnar PV cells

To situate 5-HT_{3A}R cell action within the auditory thalamocortical circuit, we next performed a series of anatomical and optogenetic electrophysiological studies. First, we exploited AAV-Brainbow technology[23]. This genetic strategy uses Cre-loxP recombination to yield stochastic combinatorial expression of fluorescent proteins to individually label cortical 5-HT_{3A}R cell morphology with distinct colors and identify potential postsynaptic targets (Fig. 2a–c). Across all cortical layers in A1, 5-HT_{3A}R cells rarely formed boutons onto pyramidal cell somata (Fig. 2d), consistent with their inhibition of calcium signals along apical dendrites[24]. In contrast, PV cell bodies in L2/3 and L4 received more 5-HT_{3A}R cell putative contacts (Fig. 2d) arising from a greater number of 5-HT_{3A}R cell axons, as distinguished by unique Brainbow-colors (Fig. 2e).

To determine the columnar and laminar organization of individual L1 cells targeting these PV cells, we further traced the dendritic and axonal arbors of 5-HT_{3A}R cells across the tonotopic axis of A1 (Fig. 2f). While their dendrites generally remained confined to superficial cortical layers, many 5-HT_{3A}R cell axons descended vertically in a narrow cortical column, contacting postsynaptic PV cell targets within a tight span in L4 (average arbor width of 23μm) along the rostro-caudal tonotopic axis (Fig. 2g).

5-HT_{3A}R cells gate a window of thalamocortical disinhibition

We then asked how these 5-HT_{3A}R interneuron projections impact the function of their L4 targets. The light-activated channel, channelrhodopsin-2 (ChR2), was expressed selectively by crossing 5-HT_{3A}R-Cre mice with floxed ChR2 (Ai32) mice (Fig. 3a,b). To determine postsynaptic targets, we recorded from morphologically and electrophysiologically identified PV and pyramidal cells within L4 of A1 in acute slices (Fig. 3b). Optogenetic activation of 5-HT_{3A}R interneurons produced fast, bicuculline-sensitive ($GABA_A$R) inhibitory postsynaptic potentials (IPSPs) in PV cells, but generally mixed $GABA_A$R and slow, $GABA_B$R (SCH-50911-sensitive) IPSPs in pyramidal cells (Fig. 3c,d). In fact, 5-HT_{3A}R cell-induced IPSPs recorded in pyramidal cells showed significantly longer half-widths and decays compared to those recorded in PV cells (Fig. 3d).

Prolonged IPSPs in pyramidal cells showed an enhanced late inhibitory phase (200–600ms; Fig 3d). Overall, this suggests that activation of 5-HT_{3A}R interneurons produces distinct

inhibition onto PV and pyramidal cells in L4. The L1 interneuron population primarily consists of LS cells targeting both dendritic $GABA_A$ and $GABA_B$ receptors, and non-LS cells targeting primarily $GABA_AR$ synapses[14]. We performed paired recordings between these $5HT_{3A}R$ cell subtypes and PV cells in L4. Only spikes in the non-LS interneurons produced inhibitory postsynaptic currents (IPSCs) in these distant targets (Fig. 3h; non-LS, 2/7 tested connections, LS, 0/8 tested connections). These cells showed irregular spiking and fast after-hyperpolarizations, similar to a L2/3 $5HT_{3A}R$ cell population identified previously[10]. These results reveal a novel connection between L1 interneurons and the PV interneurons below.

We, therefore, recorded the functional impact of 5-$HT_{3A}R$ cells on thalamic input to L4, which arrives nearby on the soma[25] (Fig. 2d). Again leveraging the auditory thalamocortical slice, we applied blue light pulses to fire single action potentials in ChR2-expressing 5-$HT_{3A}R$ cells concurrent with MGB-driven thalamic responses in PV or pyramidal cells of L4 (Fig. 3e,f). Electrical stimulation of the MGB afferents triggers large EPSPs in PV cells that generally result in action potentials. When 5-$HT_{3A}R$ cells were co-activated, the amplitude of these thalamocortical EPSPs were blunted (Supplementary Fig. 3) and PV cell spiking reduced (Fig. 3f,g) for up to 100 ms, revealing a powerful descending control of feed-forward inhibition. Consistent with this, L4 pyramidal cells responded biphasically to 5-$HT_{3A}R$ cell activation. Typically weak, sub-threshold thalamocortical EPSPs in pyramidal cells were initially enhanced, while EPSPs elicited > 100 ms after 5-$HT_{3A}R$ cell activation were robustly suppressed (Fig. 3f,g).

To explore how these descending 5-$HT_{3A}R$ cell projections shape network activity across the tonotopic axis of A1, we examined the effects of silencing these cells on MGB-driven cortical responses using voltage-sensitive dye imaging (VSDI). 5-$HT_{3A}R$ cell silencing decreased responses within L2/3 and L4 of the topographically active columns while laterally increasing responses in neighboring columns (Supplementary Fig. 4). Moreover, these effects occurred at different timescales corresponding to the distinct kinetics of IPSPs evoked in PV and pyramidal cells (Fig. 3a–d): the decrease within the MGB-activated column occurred during the early peak of the response, whereas the enhancement in neighboring columns occurred during the later phase. Thus, 5-$HT_{3A}R$ cell activation orchestrates both temporal and spatial activity patterns in A1: rapidly sharpening activity within frequency columns by inhibiting PV cells directly below, while truncating responses outside the primary column by delayed lateral inhibition of pyramidal cells.

$5HT_{3A}R$ cell silencing prevents critical period plasticity

A global tonotopic organization across the A1 rostro-caudal axis arises from the topographically-organized projections from the MGB[26,27]. We previously showed that passive sound exposure during a brief critical period (postnatal day, P12–15)[3,4] does not alter the thalamic tonotopic map, but induces robust shifts in the thalamocortical topography of L4 in mouse A1[5]. We asked whether 5-$HT_{3A}R$ interneuron activity is important for such developmental rewiring.

We silenced 5-$HT_{3A}R$ cells *in vivo* during passive tone exposure by a chemogenetic approach[28]. An adeno-associated virus (AAV) carrying the engineered G-protein-coupled

receptor transgene, hM4D(Gi)-mCherry, was injected into A1 of 5-HT_{3A}-Cre pups and Cre-negative littermate controls at P2 (Fig. 4a). To verify our silencing method, we evaluated at P12–15 the ability of the agonist, clozapine-*N*-oxide (CNO), to reduce synaptic transmission from 5-HT_{3A}R cells in A1 brain slices further expressing ChR2 (5-HT_{3A}-Cre x Ai32 mice). Optogenetic activation of 5-HT_{3A}R cells evoked IPSCs in nearby L2/3 pyramidal cells as expected. Bath application of CNO (15μM) reduced this IPSC amplitude significantly when 5HT_{3A}R cells also expressed hM4D(Gi) and increased the paired-pulse ratio (PPR) validating this approach to reduce 5-HT_{3A}R cell GABA release[28] (Fig. 4b).

To investigate the impact of such 5-HT_{3A}R cell-silencing on tonotopic plasticity, we then examined changes in connectivity between the MGB and A1 in thalamocortical slices[5,26]. Pups were exposed to a pulsed 7 kHz tone during the typical critical period from P12 to 15 concurrent with CNO (1mg/kg i.p.; 2x daily) before slicing at P20. The MGB was stimulated at six different sites along the tonotopic latero-medial axis to mimic tones at varying frequencies, and cortical responses were measured using VSDI, as described previously[5,26] (Fig. 4c,d, Supplementary Fig. 5). To quantify thalamocortical topography, we plotted the location of the peak response (ΔF/F) along the tonotopic rostro-caudal axis of cortical L4 as a function of MGB stimulation site (Fig. 4e).

A significant decrease in the slope of the topographic curve reflected plasticity following 7 kHz exposure in wildtype (C57Bl6/J) mice, as shown previously[5] (topographic slope: C57 Naïve = 1.01 ± 0.17, n = 15 mice; C57 7kHz, 0.35 ± 0.26, n = 11 mice; unpaired *t* test, t(24) = −2.22, P = 0.036, data not shown). However, 5-HT_{3A}R cell-silencing prevented this plasticity, resulting in a significant preservation of topographic slope in hM4d-expressing pups receiving CNO concurrent with tone-rearing as compared to littermate controls (Fig. 4f). Together, these results reveal that suppressing 5-HT_{3A}R cell function blocks sound-evoked thalamocortical plasticity during a developmental critical period.

Nicotinic recruitment of 5-HT_{3A}R interneurons controls critical period timing

Mechanisms underlying critical period closure in A1 are largely unknown, but seminal plasticity studies in the adult following cholinergic manipulation point to this pivotal neuromodulatory system[29,30]. Thus, we asked whether the developmental loss of tonotopic plasticity is due to changes in the cholinergic recruitment of 5-HT_{3A}R cells. We found only modest changes in gene expression for nAChR subunits within these FACS-sorted cells from A1 between P11 and P20, when tonotopic map plasticity winds down (Supplementary Fig. 6). Instead, we found a nearly 2-fold developmental increase in *Lynx1* expression that encodes an endogenous prototoxin[31] known to be expressed in cortical interneurons[32] (Supplementary Fig. 7) and inhibit nAChR function[31,32] (Fig. 5a).

Consistent with the emergence of Lynx1, nAChR sensitivity of 5-HT_{3A}R cells was attenuated in adulthood. Nicotine (bath-applied, 10μM) robustly increased spontaneous spiking of 5-HT_{3A}R cells in young critical period-aged pups (P12–15), but this effect was largely lost one week later and beyond (Fig. 5b,c). In contrast, heightened nicotine sensitivity was retained in older *Lynx1*$^{-/-}$ knockout (Lynx1 KO) mice. Nicotine further induced a barrage of inhibitory IPSCs within 5HT_{3A}R cell-target PV and pyramidal cells in the mutant mice (Supplementary Fig. 8).

These nicotine-induced IPSCs persisted in mice carrying a double deletion of genes encoding both Lynx1 and the α7 nAChR subunit or during blockade of α7-nAChRs by the selective antagonist methyllycaconitine (MLA; bath-applied, 10nM; Supplementary Fig. 8). This suggests that non-α7 subunit-containing nAChRs predominantly activate L1 cells in response to bath-applied nicotine. Indeed, pharmacological blockade of α4-containing nAChRs with the selective blocker, dihydro-β-erythroidine hydrobromide (DHβE; bath-applied, 500nM) prevented the nicotine-induced increase in IPSC frequency of Lynx1 KO mice (Supplementary Fig. 8). Thus, Lynx1 appears to regulate cholinergic activation of 5-HT_{3A}R cells through α4-containing nAChRs.

We next determined whether 5-HT_{3A}R cells need to be engaged to keep the critical period open. Mice aged one week beyond the window for tonotopic plasticity (P20–23) failed to exhibit shifts by passive sound exposure (Fig. 5d), as shown previously[5]. Administering an acetylcholinesterase inhibitor (physostigmine, 0.1mg/kg, i.p. daily[32]) to elevate cholinergic tone reopened auditory thalamocortical plasticity in wildtype mice of this age (Fig. 5d).

Similarly, Lynx1 KO mice displayed extended plasticity into older ages (Fig. 5e). To rule out a possible effect of *Lynx1* deletion on peripheral hearing, we verified that brainstem responses in Lynx1 KO mice exhibited normal auditory thresholds (Supplementary Fig. 9a–d). The ectopic plasticity persisted in mice carrying a double deletion of the genes encoding Lynx1 and α7-nAChRs (Fig. 5e), suggesting as above that α7-nAChRs are not involved. Instead, administration of DHβE (i.p. 1mg/kg; daily), which also did not alter peripheral hearing thresholds (Supplementary Fig. 9e–h), prevented the extended plasticity in Lynx1 KO mice (Fig. 5e).

Using *in situ* hybridization, we found that 90% of 5HT_{3A}R interneurons (36/40) co-expressed mRNAs encoding the *Chrna4* subunit and *Lynx1*. To establish whether nAChR activation of 5-HT_{3A}R cells is essential for the heightened plasticity in the Lynx1 KO mice, we adopted an optogenetic approach. We generated triple transgenic 5-HT_{3A}-Cre x Ai35 x Lynx1 KO mice expressing an inhibitory opsin in 5-HT_{3A}R cells, allowing us to acutely silence these cells only when each tone was played. Photo-inhibition of 5-HT_{3A}R cells *in vivo* through a cleared-skull cap abolished the sound-evoked thalamocortical plasticity in Lynx1 KO mice (Fig. 5f). Together, these studies reveal that an active down-regulation of α4-nAChR signaling in 5-HT_{3A}R cells likely contributes to the developmental loss of tonotopic plasticity.

The VIP-expressing 5-HT_{3A}R cell subtype does not regulate critical period plasticity

A subtype of 5-HT_{3A}R interneuron that selectively expresses vasoactive intestinal peptide (VIP) sends descending axons to deeper cortical layers and disinhibits pyramidal cells[12–16]. Thus, we asked whether this sub-population mediates PV cell suppression in L4 and tonotopic plasticity.

VIP interneurons, generally found in deeper layers[10,20], received some vGluT2-expressing puncta from the MGB, but received significantly fewer than those onto L1 non-VIP cells (Fig. 6a,b). Using *in situ* hybridization, we also found less mRNA encoding α4-nAChR and Lynx1 in VIP cells compared to the general 5HT_{3A}R cell population (Fig. 6c,d). Notably, a

subset of the vertically-projecting $5HT_{3A}R$ cells within superficial layers of A1 were VIP cells projecting preferentially onto PV cells (Fig. 6e,f). We selectively expressed ChR2 using VIP-Cre x Ai32 mice to optogenetically induce IPSPs in PV cells of L4. These were larger in amplitude with shorter half-widths compared to those recorded in nearby pyramidal cells (Fig. 6g–i).

Importantly, these IPSPs were smaller than those observed by activating the general $5HT_{3A}R$ population (Fig 3d), causing only a rapid, modest suppression of thalamic-driven firing in PV cells with little impact on EPSPs in pyramidal cells (Fig. 6j,k). Thus, VIP cells could contribute to intra-columnar PV cell suppression, but do not act alone to disinhibit L4. Indeed, silencing the VIP cell population alone did not significantly affect tonotopic plasticity (Fig. 6l), emphasizing a role for non-VIP cells in orchestrating this developmental critical period.

A cortical L1 map tunes auditory cortex

We finally examined the precision of thalamic input to 5-$HT_{3A}R$ cells. Topographic maps using VSDI revealed that L1 activity mirrored that in L4 upon MGB stimulation (Fig. 7a–d). This topographic organization had a linear slope in L1 similar to that observed in L4 (Fig. 7c). To further determine whether MGB innervation of 5-$HT_{3A}R$ cells in L1 is topographically-organized, we used 5-$HT_{3A}R$-Cre x Ai95 mice to express a calcium indicator (GCaMP6f) in 5-$HT_{3A}R$ cells. Stimulating discrete positions either within the medial or lateral MGB activated 5-$HT_{3A}R$ cells in rostral or caudal L1 of A1, respectively (Supplementary Fig. 10).

We next examined the origin of MGB axons projecting to cortical L1 by injecting fluorescent dyes conjugated to wheat germ agglutinin (WGA) within L1 and visualizing retrogradely transported dye-labeled vesicles within thalamus 24 h later (Fig. 7e–h). Focal, superficial injections along the rostro-caudal axis of A1 revealed a region of L1-projecting MGB cells, topographically organized along the tonotopic caudolateral to rostrolateral axis[26]. Interestingly, unlike L4, the functional topography in L1 remained intact after 7kHz tone exposure during the critical period, resulting in two overlaid yet displaced, topographic representations (Fig. 7c). Thus, 5-$HT_{3A}R$ cells in L1 constitute a stable topographic map that is poised to disinhibit thalamocortical drive and gate plasticity within the layers below.

DISCUSSION

Our studies unveil a new picture of the neuronal network of 5-$HT_{3A}R$ cells within cortical L1 (Supplementary Fig. 11). The canonical cortical circuit model relies on MBG axons terminating solely in L4. Our study reveals that these inputs extend up into L1 and robustly innervate resident 5-$HT_{3A}R$-expressing inhibitory interneurons. This is consistent with recent reports suggesting that superficially positioned interneurons may receive thalamic input[20,33] and respond to sound in A1[34]. Surprisingly, this MGB input to L1 is precise, exhibiting a topographic map across the A1 tonotopic axis that mirrors the one in L4 (Fig. 7). Recent work has revealed that the dorsal lateral geniculate nucleus also sends retinotopically-organized projections to superficial layers within the primary visual cortex that convey precise information about visual space[9], direction and orientation[8]. It will be

interesting to determine whether sensory maps in superficial cortical layers generally modulate L4 activity to guide plasticity across modalities.

Intriguingly, maps in L4 and L1 were independently controlled by early sensory experience: sound exposure robustly restructured L4, leaving L1 intact. This raises an interesting possibility that thalamocortical inputs to L4 and L1 exhibit distinct plasticity mechanisms. The excitation of L1 appears more focal than that observed in L4 (Fig. 7b,d), perhaps restricted spatially by inhibitory interactions between L1 interneurons[35]. The L1 map may thus serve as a potentially stable reference scaffold, available to rapidly mold L4 maps during periods of heightened plasticity throughout life. A similar strategy is employed in the barn owl tectum, which can acquire multiple co-existing maps of interaural time difference during development to enable rapid adaptive plasticity in adulthood[36].

Apart from being contacted by thalamic axons, 5-HT_{3A}R cells within A1 are activated by cholinergic inputs arising from the basal forebrain[11]. These afferents may preferentially relay phasic signals to 5-HT_{3A}R cells via nAChRs[10] (Fig. 1) with remarkable temporal precision in response to ethologically-relevant stimuli, such as air puffs or water rewards[37]. While generally thought to be broadcast across the extent of A1 to depolarize 5-HT_{3A}R cells homogeneously, these fast modulatory signals may serve to briefly lower the spiking threshold of L1 cells and switch on portions of the L1 map that are co-activated by precise MGBv inputs. This circuit organization identifies L1 interneurons as hubs for integrating diffusely projecting contextual signals with specific sensory stimuli. Thus, 5-HT_{3A}R cells are uniquely poised to translate global changes of neuromodulation into focal plasticity.

The 5-HT_{3A}R cells have been shown to act within various circuits across the cortex[10–17]. We here revealed a direct connection from L1 interneurons onto L4 PV interneurons. By differential targeting of subcellular domains and use of distinct postsynaptic inhibitory timescales, 5-HT_{3A}R cells differentially impact thalamic drive onto PV and neighboring pyramidal cells in L4. Precisely timed activation of L1 interneurons suppressed thalamic-driven spikes in PV cells, thereby disinhibiting pyramidal cells (Fig. 3). Consequently, L1 interneuron activation generates time windows of enhanced thalamic drive onto L4 pyramidal cells that may support the induction of spike timing-dependent plasticity (STDP), a potential mechanism underlying sound-evoked shifts in A1 tuning[38]. Thus, the relative timing of L1 and L4 activation may be a key determinant of plasticity.

It is important to note that 5-HT_{3A}R interneurons are a heterogenous population. These may act in various ways to constrain cortical activity and plasticity in a temporo-spatially precise manner. While the two major subtypes, LS and non-LS interneurons, were both robustly activated by MGB inputs (Fig 1), they may act on different postsynaptic elements. The LS subtype often targets dendritic $GABA_A$ and $GABA_B$ receptors, and thus likely produces the prolonged $GABA_B$ receptor-mediated inhibitory potentials we observed in pyramidal cells. These interneurons send lateral projections and may act to reduce prolonged activity outside the cortical column (Supplementary Fig. 4). Conversely, the non-LS subtype sends narrowly descending projections, targeting $GABA_A$ receptors on PV interneurons within L4 (Fig. 2,3).

A subset of these non-LS cells expressing VIP is also found in deeper cortical layers, where they target both somatostatin and PV interneurons[12–16]. VIP cells received fewer vGluT2-expressing puncta than non-VIP cells (Fig. 6), consistent with recent optogenetic studies showing only weak thalamic innervation of VIP cells[20]. VIP cells also expressed fewer mRNAs encoding α4-nAChR subunits (Fig 6) and may instead express more 5-HT_{3A}Rs[39], suggesting that VIP and non-VIP cells are engaged by distinct neuromodulators. Silencing VIP interneurons, however, did not impact critical period plasticity significantly in A1, consistent with recent observations in visual cortex indicating no role before P30 [40]. Together, these findings point to a non-LS subtype lacking VIP as the pivotal player in A1 development. Future studies identifying molecular markers for L1 interneuron subtypes with distinct connectivity patterns will be important for determining their separate roles in regulating cortical plasticity.

Seminal work in kitten visual cortex indicates a combined requirement for noradrenergic and cholinergic fibers in ocular dominance plasticity[6]. Cholinergic inputs target diverse cortical cell populations to influence network activity through both ionotropic nAChR and G-coupled muscarinic receptors. Notably, both nicotinic disinhibition and muscarinic enhancement of thalamic glutamate release by suppression of adenosine signaling may act synergistically to induce thalamocortical plasticity in mature A1[41]. Although all cholinergic actions must be considered, young 5-HT_{3A}R cells in L1 are rapidly and robustly activated through ionotropic nAChRs (Fig. 5). These interneurons express both α4 and α7 subunit-containing nAChRs (Fig. 1)[42], but the former mediates the strong nicotine-induced spiking of these cells (Fig. 5, Supplementary Fig. 8). While α7-nAChRs quickly desensitize and contribute only transiently to 5-HT_{3A}R interneuron activation, α4-nAChR signaling was adequate for tonotopic plasticity (Fig. 5) and may likewise play a key role in the deprivation-induced plasticity of mouse somatosensory cortex[43]. Notably, cholinesterase inhibitors, which reopen periods of A1 plasticity beyond early life (Fig. 5d), selectively augment α4-nAChR responses[40]. The developmental reduction of α4-nAChR signaling by the appearance of Lynx1 within 5-HT_{3A}R cells (Fig. 5a–c) may then explain how this protein serves as a cortical plasticity ‘brake’[1,32].

To date, the impact of 5-HT_{3A}R cells on the developing cortex had largely been ignored. Here, we find that they may serve as endogenous regulators of PV cells and hence critical period plasticity. This may explain in part how perinatal exposure to serotonin reuptake inhibitors might accelerate plastic windows for phoneme discrimination in human infants[1]. Transient periods of reduced synaptic inhibition precede A1 receptive field plasticity *in vivo*[30], and a rapid reduction of PV cell spike rates precedes ocular dominance plasticity in the visual cortex during the critical period[44]. Reversible shifts in PV cell state correlate with adult hippocampal learning[13], while pharmacological re-setting of PV cells reopens visual plasticity[45].

Studies in mature A1 have instead focused on neuromodulatory influences[11,29–30]. Direct (basal forebrain)[29,30] or indirect (vagal nerve) stimulation[46] of cortical cholinergic release promotes adult auditory plasticity. Behavioral training using rewarding or aversive stimuli, known to rapidly engage cholinergic afferents[37] and 5-HT_{3A}R cells[10,11,15], also drives tone-evoked shifts in adult tonotopic maps[47]. More recently, cholinergic signaling has been found

to engage 5-HT$_{3A}$R cell activity across cortical areas[11,16], and facilitate adult plasticity in both visual[32,48] and auditory systems[11,30] (Fig. 5).

Our findings thus resolve a link between two long-standing models of cortical plasticity (PV cell function and neuromodulation) through L1 cells. Engaging contextual signals paired with training is needed to enhance plasticity even in early development. Brief exposure to structured communication during infancy results in phonetic learning, but this requires social interaction with a tutor both in humans[2] and songbirds[49]. By leveraging the L1 map to promote specific plastic change, neuromodulators as well as inputs from diverse thalamic[7–9] or cross-modal cortical areas[50], may influence early auditory critical periods. How and when the L1 map can be engaged throughout life holds key insights for educational and therapeutic strategies where heightened plasticity is desirable.

Data availability

All data relevant to this work will be made available upon request.

ONLINE METHODS

Mice

Wild-type (C57Bl6/J; JAX 000664), PV-IRES-Cre[51] (B6;129P2-Pvalb$^{tm1(cre)Arbr}$/J; JAX 008069), SOM-IRES-Cre[52] (SST$^{tm2.1(cre)Zjh}$/J; JAX 013044), VIP-IRES-Cre (VIP $^{tm1(cre)Zjh}$/J; JAX 010908)[52], Ai35[53] (B6;129S-Gt(ROSA)$^{26Sortm35.1(CAG-aop3/GFP)Hze}$/J; JAX 012735), Ai32[53] (ChR2(H134R)-EYFP; JAX 012569), and Ai95[54] ((RCL-GCaMP6f)-D; JAX 024105) breeders were purchased from Jackson Laboratories. 5-HT$_{3A}$R-Cre (Tg(Htr3a-cre)NO152Gsat/Mmucd; MMRRC) breeders were purchased from MMRRC. Lynx1 knockout (KO)[31] breeders were provided by J. Miwa (LeHigh University) and Lynx1 KO x α7-nAChR KO[55] breeders were provided by H. Lester (California Institute of Technology). PV-GFP[56] transgenic mouse breeders were provided by H. Monyer (Heidelberg University). All mice were raised from breeding pairs in our colony and housed with up to four littermates under standard laboratory conditions (12:12 h light:dark cycle, access to water and food *ab libitum*). Both male and female mice were used for experiments. Animal care and experimental procedures were performed in accordance with protocols approved by the Harvard University Institutional Animal Care and Use Committee and the Boston Children's Hospital Institutional Animal Care and Use Committee.

Brainbow Expression in 5-HT$_{3A}$R cells and Imaging

5-HT$_{3A}$R-Cre mice (P41–42; 2 male and 2 female) were injected with the Brainbow virus[23] in the primary auditory cortex (A1). Mice were anesthetized with isoflurane and prepared for surgery using sterile technique. Using a stereotaxic apparatus, a craniotomy was made above A1, 2.5mm posterior to Bregma and 4.5mm lateral to the midline. Three superficial (300μm below pial surface) injections were made within the left hemisphere of A1 (500nL/injection site) using a 10μL Hamilton syringe (Hamilton, 765301) with a motorized piston (Narishige; speed ~ 25nL/min). To label MGB projections to 5-HT$_{3A}$R interneurons, adult 5-HT$_{3A}$R-Cre mice (>P60; 2 male and 2 female) were injected with one Brainbow virus in A1 as described above and the other Brainbow virus combined with Cre (1:10,000) in the MGB

(1μL/injection site; 3.28mm posterior to Bregma, 2.0mm lateral to the midline and 3.25mm below pial surface). The head wound was sutured, and mice were immediately administered an injection of the nonsteroidal anti-inflammatory agent meloxicam. Following a period of recovery on a heating pad with accessible food pellets and HydroGel, the mice were returned to their home cages. The mice were administered a second dose of meloxicam the following day.

Following 3 weeks of infection, mice were perfused intracardially with saline followed by 4% PFA in 0.1M PB and then post-fixed overnight at 4ºC. Brains were washed in PBS and sectioned perihorizontally (60–100μm). Sections were blocked in StartingBlock (ThermoScientific; 95%, with 4% PBS & 1% Triton-X-100) for 1hr at room temperature (RT), then washed in PBS-T (PBS with 0.25% Triton-X-100) before 5 nights of 4ºC incubation in the following primary antibody cocktail : a base of 0.02%-NaN3 PBS with 1% Triton-X-100, chicken anti-GFP (Abcam, ab13970; 1:2000), and 3 custom-made antibodies from Covance (rabbit anti-mCherry, guinea pig anti-mKate2, & rat anti-mTFP1.0). Other primary antibodies used were mouse anti-Parvalbumin (Swant, 235; 1:300), rabbit anti-vasoactive intestinal protein (Immunostar, 20077; 1:200), guinea pig anti-vesicular glutamate transporter 2 (vGluT2; Synaptic Systems, 135404; 1:500), and goat anti-choline acetyltransferase inhibitor (ChaT; Millipore, AB144P; 1:100). Sections were washed in PBS-T and incubated for 2 nights at 4ºC in secondary antibodies. Secondary antibodies used were DyLight-conjugated donkey anti-rabbit 405 (Jackson ImmunoResearch, 1:500 711-475-152), and alexa dye-conjugated goat anti-chicken 488 (A-11039), goat anti-mouse 546 (A-11030), goat anti-rat 594 (A-11007), and goat anti-guinea pig 647 (A-21450), goat anti-mouse 488 (A-11001), goat anti-rabbit 546 (A-11010), goat anti-guinea pig 594 (A-11076), goat anti-chicken 647 (A-21449), donkey anti-goat 546 (A-11056), and donkey anti-rat 594 (A-21209; Life Technologies, 1:500). Finally, sections were washed in PBS-T, incubated for 30 m at RT in 1:350 NeuroTrace 435/455 (Life Technologies) in PBS-T, and mounted using ProLong Gold (Life Technologies).

Images for analysis of Brainbow-labeled 5-HT_{3A}R cell inputs were acquired on a Zeiss LSM 710 confocal using a 63x, 1.4NA oil immersion PlanAPO objective (1.1x zoom), with voxels sized 94nm in XY and with a 250nm Z-step, and with optical sections of ~0.6μm / channel (12-bits; 16x line-averaging). Images for reconstruction of Brainbow-labeled cells were acquired using a 40x, 1.3NA oil immersion PlanAPO objective (1.1x zoom). Images were corrected for chromatic aberration in three dimensions using a custom ImageJ/Fiji plugin (D. Cai, U Michigan) and global pixel-shift values determined from a set of single antibody, multi-label images acquired using the same settings.

To quantify Brainbow-labeled 5-HT_{3A}R cell inputs to PV+ and pyramidal cell bodies, boutons apposed to NeuroTrace-labeled somata were manually counted using ImageJ/Fiji (Version: 2.0.0-rc-15/1.49i). Boutons were identified morphologically as a swelling of the axon, and only appositions lacking dark pixels between the bouton and the cell body profile were considered[57]. All boutons apposed to the cell body throughout its 3D extent were counted, and only cells fully contained within the stack were analyzed. Like-colored axonal segments were tracked back to a branch point to check if they were part of the same axon (i.e., a terminal fork[58]), and were further disambiguated by toggling the display of the 4th

Brainbow-channel – usually left un-visualized on 3-color RGB displays – to further enhance color diversity. To quantify thalamic innervation of 5-HT_{3A}R interneurons, vGluT2+ boutons apposed to VIP+ or VIP− NeuroTrace-labeled somata were counted. All boutons on the single z-plane in which the 5-HT_{3A}R interneuron somata was largest were counted.

Whole-cell Recordings

Mice were anesthetized with isoflurane and decapitated. The brain was quickly removed in chilled oxygenated ACSF containing (mM): 125 NaCl, 25 glucose, 25 $NaHCO_3$, 2.5 KCl, 2 $CaCl_2$, 1.25 NaH_2PO_4 and 1 $MgCl_2$. Thalamocortical slices (300–600 μm) were sectioned on a vibrating microtome (Leica Microsystems, VT1200S) and incubated at room temperature until placed in a recording chamber. Patch pipettes (4–6 MΩ) were pulled with a DMZ micropipette puller (Dagan Corporation). Whole-cell capacitance was compensated and the initial series resistance was compensated about 60%. Data were acquired from cells with a resting potential less than −55 mV, an initial series resistance < 20 MΩ, and overshooting action potentials. Data were collected at a sampling rate of 10 kHz using an Axopatch 1D or 700B amplifier (Axon Instruments), low-pass filtered at 2 kHz, and digitized using an ITC-18 (InstruTech). Recordings were performed at room temperature (22–24°C). Custom-designed IGOR (WaveMetrics, Version 6.36) programs were used for data acquisition and analysis[59]. All electrophysiological analyses were performed blind to the age, genotype, cell type, or drug condition.

To measure excitatory post-synaptic potentials (EPSPs) evoked by pressure application of nicotine or m-CPBG (100μM) in 5-HT_{3A}R cells in cortical L1, whole-cell current-clamp recordings were performed in adult (>P60) male and female mice. The current-clamp internal solution contained (mM): 7 KCl, 135 K-gluconate, 10 HEPES, 4 Mg_2ATP, 0.4 GTP sodium salt, 10 phosphocreatine disodium salt (pH = 7.2 with KOH). Whole-cell current-clamp recordings were also used to measure the effects of nicotine on spontaneous spiking of 5-HT_{3A}R cells in cortical L1. For these experiments, the ACSF was modified to contain 3.5mM KCl and 0.5mM $MgCl_2$ to enhance spontaneous activity. Following a 450s baseline measurement, nicotine was bath-applied (10μM) for 900s, and then washed out for 900s. The nicotine effect was calculated as the peak spiking response (bins of 100s) during nicotine application divided by the mean spiking rate across the whole recording period. Only cells showing spontaneous spiking responses were analyzed. To measure the effects of bath-applied nicotine (10μM) on spontaneous inhibitory post-synaptic currents (IPSCs), whole-cell voltage-clamp recordings were obtained from L4 PV-expressing cells and L5 PYR cells (V_{HOLD} = −40mV). PV-cells were identified by the expression of GFP in PV-GFP transgenic animals. L5 PYR cells were visually identified in C57BL6/J mice by their soma shape under infrared differential interference contrast (IR-DIC). The nicotine effect was calculated as the peak sIPSC frequency (bins of 100ms) during nicotine application, divided by the baseline sIPSC frequency. In some experiments, MLA (10nM) and DHβE (500nM)[60–62] were continuously bath-applied throughout the experiment, starting 15 minutes before baseline IPSC measurements were obtained. sIPSCs were analyzed offline using MiniAnalysis Program (Synaptosoft, Version 6.0.7).

To compare the MGB-evoked EPSPs in L1 5-HT_{3A}R cells and L4 pyramidal cells, whole-cell current-clamp recordings were performed in these cells within auditory thalamocortical slices. Pulses of electrical stimulation were delivered to the fibers arising from the MGBv (0.5ms) with an ACSF-filled glass pipette and a constant current stimulus isolator (Iso-Flex, A.M.P.I.). Minimum-evoked EPSPs were collected using an MGBv stimulus intensity that evoked about 50% failures. Only successful EPSPs were analyzed. Maximum-evoked EPSPs were averaged over 10 trials obtained at a rate of 0.05 Hz. Short-term plasticity was evaluated by delivering trains of stimuli to the MBGv afferents (10 pulses, 0.5ms, 10 and 20 Hz).

Optogenetic experiments were performed in auditory thalamocortical slices from 5-HT_{3A}R-Cre and VIP-Cre x Ai32 mice. Whole-cell current-clamp recordings were obtained from 5-HT_{3A}R cells in cortical L1, and L3/4 pyramidal and fast-spiking cells. Neurons were visually identified as pyramidal-shaped under IR-DIC or PV cells as large, multi-polar cells with fast-spiking (>100Hz) responses to intrinsic current injections (50–800pA). Inhibitory postsynaptic potentials (IPSPs) were recorded in PV and pyramidal cells during laser light pulses (5 ms; IkeCool 473nm laser; 20μm fiber; 2.5mW) directed towards L1. In some cells, we examined the $GABA_A$ or $GABA_B$ receptor-mediated components of these responses using the antagonists, bicuculline (5μM, Sigma-Aldrich) or SCH-50911 (10μM, Tocris Bioscience), respectively. We identified L1 on the basis of sparsely distributed cells using IR-DIC to visualize cell density. Recordings in 5-HT_{3A}R cells showed that this light pulse reliably activates single action potentials in these cells.

To evaluate the effects of such inhibition on thalamic-evoked responses, the intervals between optogenetic activation of the 5-HT_{3A}R cells and MGBv stimulation were randomly varied between 0 and 1000ms. The effects of 5-HT_{3A}R cell activation was evaluated for each interval, comparing alternate trials in which the laser light used to activate 5-HT_{3A}R cells was turned on or off. For the PV cell recordings, a MGBv stimulus intensity 10% above (suprathreshold) or 10% below (subthreshold) the threshold intensity required to elicit a spike was used. For the pyramidal cell recordings, in which MGBv-evoked stimulation only elicited subthreshold EPSPs[63], a laser intensity was used that elicited the maximum EPSP amplitude. Ten trials were averaged for each stimulus presentation obtained at a rate of 0.05Hz.

To examine connections between L1 and PV interneurons, paired recordings were performed. Brief pulses of intrinsic current injections (5ms, 100–300pA) elicited single spikes in pre-synaptic L1 interneurons recorded in current-clamp, and the resulting IPSCs were recorded in post-synaptic L4 PV interneurons recorded in voltage-clamp. The voltage-clamp internal solution contained (mM): 100 KCl, 40 K-gluconate, 8 NaCl, 10 HEPES, 2 MgCl2, 0.1 EGTA, 2 adenosine 5′-triphosphate disodium salt (ATP), 0.3 guanosine 5′-triphosphate sodium salt (GTP), and 5 lidocaine derivative QX-314 (pH = 7.2 with KOH). This internal solution contains a high chloride concentration to obtain IPSCs at a holding potential of −60 mV.

To verify our method of 5-HT_{3A}R chemogenetic cell silencing, we examined the effects of CNO in reducing 5-HT_{3A}R cell synaptic transmission in A1 slices from 5-HT_{3A}-Cre x Ai32

mice aged P12–15 that had been injected with hM4d(Gi) at P2. Whole-cell voltage-clamp recordings using high chloride internal solution were used to record IPSCs in L2/3 pyramidal cells during optogenetic activation of 5-HT_{3A}R cells. Optogenetic activation was achieved by pairs of laser light pulses (5 ms; IkeCool 473nm laser; 20μm fiber; Inter-stimulus-interval = 80 ms) directed towards L1. The light stimulus intensity used was 2x the threshold intensity required to elicit an IPSC. IPSC amplitude and paired-pulse ratio were averaged across ten trials (obtained at 0.05 Hz) at baseline and 15m following CNO (15μM) bath-application. Cre negative x Ai32 littermates were used as controls. The acquisition and analysis were performed blind to the mouse genotype.

Flourescence-Activated Cell Sorting (FACS) and Real-Time quantitative PCR (RT-qPCR)

Mice were anaesthetized with isoflurane, decapitated, and the auditory cortex was isolated immediately. We then used a trehalose-supplemented protocol[64] to isolate EGFP-labeled 5-HT_{3A}R-, PV-, or SOM-expressing cells using the corresponding Cre lines. Digestion and dissociation were performed using the Papain Dissociation System (Worthington Biochemical Corporation) in the presence of 10% (vol/vol) D-trehalose (Sigma-Aldrich). Digested tissue was dissociated with measured trituration to obtain a single cell suspension of mostly viable cells. GFP-positive cells were collected using MoFlo (Beckman Coulter) in the Bauer Core Facility at Harvard University and total RNA was extracted using TRIzol Reagent (Invitrogen) and RNeasy Micro Kit (Qiagen). cDNA was synthesized from total RNA using the High Capacity RNA-to-cDNA Kit (Invitrogen) according to the manufacturer's instructions. Real-time quantitative PCR was performed using the TaqMan Gene Expression Assay (Applied Biosystems) on a StepOnePlus Real-Time PCR System (Applied Biosystems). TaqMan probes used were for *Lynx1* (Mm01204957_g1), *Chrna4* (Mm00516561_m1), *Chrna7* (Mm01312230_m1), *Chrnb2* (Mm00515323_m1), *HTR3A* (Mm00442874_m1) and *Gapdh* (4352932E). Relative expression of target genes was quantified using the $2^{-\Delta\Delta Ct}$ method[65].

In vitro Voltage-Sensitive Dye Imaging (VSDI) and GCaMP imaging

Thalamocortical topography was evaluated using a previously described *in vitro* method[5,26]. The brain was rapidly removed in chilled oxygenated artificial CSF (ACSF) containing (mM): 119 NaCl, 20 glucose, 26.2 $NaHCO_3$, 2.5 KCl, 2.5 $CaCl_2$, 1 NaH_2PO_4 and 1.3 $MgCl_2$. Thalamocortical slices were then generated by sectioning the brain perihorizontally (600μm, 15°) on a vibrating microtome (Leica Microsystems) to preserve the ventral medial geniculate (MGBv) and its projection to A1, as previously described[5,26,66]. The slices were incubated for 15 min at 35°C, and then 90 minutes in the voltage-sensitive dye, Di-4-ANEPPS (Invitrogen D-1199, 5 μg/ml) at room temperature (20–22°C). Six sites in the MGBv along the latero-medial tonotopic axis spaced at 100 μm intervals were stimulated (0.5 mA, 1 ms pulse) with an ACSF-filled glass pipette and delivered with a constant current stimulus isolator (Iso-Flex, A.M.P.I.) controlled by a programmable pulse generator (MiCam Ultima Software, Version 1002). Excitation light from a shuttered 150-W halogen lamp (MHF-G150LR, Moritex) was band-pass filtered (515 and 535 nm) and reflected toward the sample by a 570-nm dichroic mirror. Emitted fluorescence was long-pass filtered (590 nm) and imaged using a MiCam Ultima CMOS-based camera (SciMedia; 1 ms frame rate; 512 ms period).

Fluorescent signals were integrated across regions of interest (125 x 125 μm) at a constant depth from the pia corresponding to layer 1 (L1; 25–150 μm from pial surface) or upper L4 along the rostro-caudal axis tonotopic of A1, standardized across slices using an anatomical landmark (most rostral point of hippocampus). Time course traces were averaged across 10 trials and exported to Igor Pro (WaveMetrics, Version 6.36) and Matlab (MathWorks, Version R2017a) for analysis. Fluorescence change was normalized to resting fluorescence (ΔF/F), and variations in stimulation intensity across MGBv sites were normalized by the maximum response within the white matter directly above the cortex. Variations in slice preparations were normalized by dividing all signals by the maximum response within cortical L4 measured across all stimulation sites within a slice. Peak ΔF/F was determined as the maximum average response within a time window (20–40 ms following stimulation) across all L4 locations. Topographic slopes for each animal were calculated as the linear relation of the position of peak ΔF/F along the rosto-caudal tonotopic axis of A1 as a function of MGBv stimulation location.

To verify our *in vivo* method of optogenetic 5-HT_{3A}R cell silencing and assess the effects on A1, VSDI experiments were performed at P12–15 in 5-HT_{3A}R-Cre x Ai35 pups. Responses to MGBv stimulation (0.5 mA, 1 ms pulse) were examined across A1 using VSDI during the presence and absence of long laser light pulses (IkeCool 595nm laser; 20μM fiber) directed towards L1. The location within L4 across the A1 rostro-caudal axis showing the maximal response was designated as the activated column. When possible, VSDI acquisition and analysis were performed blind to genotype/condition (5-HT_{3A}R cell silencing experiments, AchEI and DHβE experiments).

For GCaMP imaging, thalamocortical slices were generated from 5-HT_{3A}R-Cre x Ai95 mice (P15–22) that express the genetically-encoded calcium indicator (GCaMP6f) in the 5-HT_{3A}R cells. Sites within the lateral or medial MGBv were stimulated (0.5 mA, 1 ms pulse), and imaged as described above except with a 497nm excitation / 535 emission filter. Fluorescent signals were integrated across regions of interest (125 x 125 μm) at a constant depth from the pia corresponding to layer 1 (L1; 25–150 μm from pial surface) using the methods described above.

Sound exposure

Mice were placed in a sound-attenuating chamber (IAC) and passively exposed to 7 kHz tones (100-ms pulses at 5 Hz for 1 s, followed by 2 s of silence, 78 dB SPL[5,67,68]). A 7-kHz frequency was chosen as the middle of the sound spectrogram for mouse pup wriggling calls[69], and thus ethologically relevant for mice of this age. Mice were otherwise reared under standard conditions (12:12 h light:dark cycle, access to water and food *ab libitum*). Tones were generated by Audacity software (http://audacity.sourceforge.net/, Version 2.1.2) and delivered by speakers placed in two corners of the chamber. Mouse pups tone-exposed during the critical period (P12–15) were placed in the sound-attenuating chamber and exposed with their mothers, and then returned to standard housing conditions until P20. Some mice were administered a cholinesterase inhibitor (AChEI; physostigmine, Sigma-Aldrich, i.p. 0.1mg/kg; daily[32]), or an α4-containing nAChR antagonist, Dihydro-β-

erythroidine hydrobromide (DHβE; Tocris Biosciences, i.p. 1mg/kg; daily) during sound exposure.

5-HT_{3A}R and VIP cell silencing

For *in vivo* chemogenetic silencing, P2 5-HT_{3A}R-Cre or VIP-Cre mouse pups and Cre-negative littermate controls were cryoanaesthetized and injected with AAV-hSyn-DIO-hM4D(Gi)-mCherry (UNC; 300nL) in superficial layers of the left primary auditory cortex (A1) using a 10μL Hamilton syringe (Hamilton, 765301) with a beveled needle and a motorized piston (Narishige; speed ~ 50nL/min). To activate the hM4D(Gi) receptor, Clozapine-N-oxide (CNO; Tocris) was administered (i.p. 1mg/kg, 2x daily) during sound exposure (P12–15). To verify our method of silencing[28], 5-HT_{3A}R-Cre x Ai32 pups and Cre negative Ai32 littermate controls were injected with AAV-hSyn-DIO-hM4D(Gi)-mCherry at P2 and *in vitro* experiments were performed at P12–15.

For *in vivo* optogenetic silencing, the clear skull procedure[70] was performed on P20 mice. Mice were anesthetized with isoflurane and prepared for surgery using sterile technique. Using a stereotaxic apparatus, a small incision was made in the skin above the primary auditory cortex, 2.5mm posterior to Bregma and 4.5mm lateral to the midline. A thin layer of cyano-acrylate glue (Krazy glue) was applied to the skull. Once dry, this was covered with a thin layer of clear dental cement (Ortho-Jet). The area was then polished and a layer of clear nail polish was applied (Electron Microscopy Sciences, 72180) to reduce light glare. Finally, a plastic sheath was secured with glue (Loctite) and dental cement to allow an optical fiber (20μm, Doric) to be mounted above the auditory cortex. Animals were placed in a sound-attenuated chamber, and the optical fiber was connected to an LED using a rotary joint (Doric connectorized dual LED, LEDC2-B/A_FC), which permitted animals to move freely about the cage. During sound exposure, light pulses were delivered (595nm; 4mW measured at skull surface) during the 1s delivery of tones to silence 5-HT_{3A}R cells in 5-HT_{3A}R x Lynx1KO x Ai35 mice. Control experiments were performed in 5-HT_{3A}R x Lynx1KO x Ai35 littermates stimulated by blue (473nm) light or Cre negative Lynx1KO x Ai35 littermates stimulated by 595nm light.

RNA *in situ* hybridization

Adult male C57 mice (P102) were anesthetized by isoflurane and decapitated. The brains were rapidly removed and frozen in medium (Tissue-Tek) on dry ice. Coronal brain slices (25μm) containing A1 were cut with a cryostat (Leica CM 1900), adhered to SuperFrost Plus slides (VWR), and immediately refrozen on dry ice. *In situ* hybrization was performed using the protocol provided by the RNAscope Multiplex Assay manual (Advanced Cell Diagnostics). The following fluorophore-conjugated RNAscope probes were used: Mm-Lynx1-C1 (Cat No. 449071), Mm-Htr3a-C2 (Cat No. 411141), Mm-VIP-C2 (Cat No. 415961), and Mm-Chrna4-C3 (Cat No. 429871). Confocal images were acquired with a Zeiss LSM 710 confocal using a 63x, 1.4NA oil immersion PlanAPO objective (1.1x zoom).

Auditory Brainstem Responses (ABR) and Distortion Product Otoacoustic Emissions (DPOAE)

Adult (>P60) mice were anesthetized with 100mg/Kg ketamine and 10mg/Kg xylazine, and placed in a sound chamber lined with anechoic foam. Three needle electrodes were placed subdermally: 1) behind the right ear pinna (recording electrode); 2) at the dorsal midline between the ears (reference electrode), and 3) at the base of the tail (common ground). ABR potentials were elicited by presenting 5ms tone pips (0.5 ms rise-fall, with a $\cos^2$ envelope, at 40/s) at frequencies ranging from 5.6kHz to 32kHz to the right ear. The response was amplified (10,000x), filtered (0.1–3 kHz), and averaged with an analog-to-digital board in a PC-based acquisition system (EPL Acoustic system, MEEI, EPL Cochlear Function Test Suite; Labview). Sound pressure level (SPL) was increased in 5dB steps from 10 to 80dB. ABR waveforms were averaged from 512 presentations of the tone in alternating phase. The ABR threshold was defined as the minimal SPL that evoked a response by visual inspection.

DPOAEs in response to two primary tones of frequency f1 and f2 were recorded at 2f1–f2, with f2/f1 = 1.2 and the f2 level 10dB lower than the f1 level. Ear-canal sound pressure was amplified and digitally sampled at 4μs intervals. Fast Fourier transforms (FFT) were computed from averaged waveforms of ear canal SPL, and the DPOAE amplitude was extracted at 2f1–f2. The background level of ambient noise was measured, defined as the average of six points in the FFT on either side of the 2f1–f2 frequency and surrounding noise. Iso-response curves were performed in 5dB steps of f1 level. Threshold was defined as the f1 level required to produce a DPOAE signal at 0 dB SPL.

Stimuli were generated with 24-bit digital I–O cards (National Instruments PXI-4461) in a PXI-1042Q chassis, amplified by an SA-1 speaker driver (Tucker–Davis Technologies, Inc.), and delivered from two electrostatic drivers (CUI CDMG15008-03A). An electret microphone (Knowles FG-23329-P07) was used to monitor ear-canal sound pressure. The Auditory Wave Analysis software (https://bitbucket.org/bburan/auditory-wave-analysis/src, Version 1.0.0.6) was used for ABR analysis.

To determine whether DHβE affects peripheral hearing, ABR and DPOAE measurements were performed in Lynx1 KO mice before and 30 minutes after administration of DHβE (i.p. 1mg/kg).

Labeling of retrogradely-transported vesicles from cortical L1

Fluorescent dyes (488, 555, 594, or 647) conjugated to wheat germ agglutinin (WGA)[71] were sterotaxically injected into layer 1 within A1 of adult C57Bl6/J mice (>P60; 3 male and 3 female). Four superficial (~50μm below pial surface) injections were made within the left hemisphere of A1 (100nL/injection site) along the rostral-caudal tonotopic axis (2.2mm–3.5mm posterior to Bregma) using glass pipettes pulled with a DMZ micropipette puller attached to a 5μL Hamilton syringe with a motorized piston (speed ~ 25nL/min). The head wound was sutured, mice were immediately administered an injection of meloxicam, and recovered on a heating pad with accessible food pellets and HydroGel. The mice were returned to their home cages, and 24 h later were were perfused intracardially with saline followed by 4% PFA in 0.1M PB and then post-fixed overnight at 4°C. Brains were washed

in PBS, and thalamocortical slices (100 μm) were sectioned on a vibrating microtome (Leica Microsystems, VT1200S). Sections were incubated for 2 h at RT in 1:200 NeuroTrace 435/455 (Life Technologies) in PBS-T, and mounted using ProLong Gold (Life Technologies). Images were acquired on a Zeiss LSM 710 confocal using a 40x, 1.3NA oil immersion PlanAPO objective (1.1x zoom).

Statistical analyses

Statistical tests were performed using JMP statistical software (SAS Institute, Version JMP Pro 12). For two-group comparisons, statistical significance was determined by the two-tailed unpaired Student's *t* test for data distributed normally or the non-parametric two-tailed Mann-Whitney *U* test for data not distributed normally. For comparison across groups with unequal variance, the unequal variance t-test using an unpooled standard error was performed. Multi-group comparisons were performed using one-way ANOVA followed by Dunnett's corrected test with a control (parametric) or Kruskal-Wallis followed by Steel's corrected test (non-parametric) with a control. A multivariate ANOVA was used to test for genotype differences in ABR hearing thresholds across tonal frequencies. A paired *t* test was used to evaluate the acute effects of silencing 5-HT_{3A}R cells on VSDI responses. The Shapiro-Wilk test was used to test for normality, and Levene's method was used to test for equal variance. P values less than 0.05 were considered statistically significant.

Supplementary Material

Refer to Web version on PubMed Central for supplementary material.

Acknowledgments

We thank J. Miwa (Lehigh University) for providing the original Lynx1 KO breeders and Lynx1 KO x α7-nAChR KO mice (c/o A. Beaudet, Baylor University), H. Monyer (Heidelberg University) for the original PV-GFP mice, M. Fagiolini for comments and discussions, A. Covello and M. Snyder for assistance with Brainbow tracing, A. Castros and E. He for assistance with immuno-cytochemistry quantification and *in situ* hybridization, A. Galvin for ABR measurements to test DHβE effects, T. Barkat, E. Diel, H. Lee, R. Reh, S. Mierau, A. Patrizi, D. Cai, G. Corfas, J. Holt, G. Géléoc, A. Thompson, and C. Chen, for technical assistance and discussions, and N. De Souza, M. Nakamura, H. Bond, E. Centofante, and M. Marcotrigiano for animal care. This work was supported by the Nancy Lurie Marks Family Foundation and the Canadian Institute for Advanced Research (CIFAR; to A.E.T.), the Ellison Medical Foundation and NIMH Silvio O Conte Center (P50MH094271; to T.K.H.).

References

1. Werker JF, Hensch TK. Critical Periods in Speech Perception: New Directions. Annual Review Psychol. 2015; 66:23.1–23.24.
2. Kuhl PK, Tsao FM, Liu HM. Foreign language experience in infancy: Effects of short-term exposure and social interaction on infant learning. PNAS. 2003; 100:9096–9101. [PubMed: 12861072]
3. de Villers-Sidani E, Chang EF, Bao S, Merzenich MM. Critical period for spectral tuning defined in the primary auditory cortex (A1) in the rat. J Neurosci. 2007; 27:80–9.
4. Insanally MN, Köver H, Kim H, Bao S. Feature-dependent sensitive periods in the development of complex sound representation. J Neurosci. 2009; 29:5456–5462. [PubMed: 19403813]
5. Barkat TR, Polley DB, Hensch TK. A critical period for auditory thalamocortical connectivitiy. Nat Neurosci. 2011; 14:1189–1194. [PubMed: 21804538]
6. Bear MF, Singer W. Modulation of visual cortical plasticity by acetylcholine and noradrenaline. Nature. 1986; 320:172–6. [PubMed: 3005879]

7. Cruikshank SJ, et al. Thalamic control of L1 circuits in prefrontal cortex. J Neurosci. 2013; 32:17813–17823.
8. Cruz-Martín A, et al. A dedicated circuit links direction-selective retinal ganglion cells to the primary visual cortex. Nature. 2014; 507:358–61. [PubMed: 24572358]
9. Roth MM, et al. Thalamic nuclei convey diverse contextual information to layer 1 of visual cortex. Nat Neurosci. 2015; 19:299–307. [PubMed: 26691828]
10. Lee S, Hjerling-Leffler J, Zagha E, Fishell G, Rudy B. The largest group of superficial neocortical GABAergic interneurons expresses ionotropic serotonin receptors. J Neurosci. 2010; 30:16796–808. [PubMed: 21159951]
11. Letzkus JJ, et al. A disinhibitory microcircuit for associative fear learning in the auditory cortex. Nature. 2011; 480:331. [PubMed: 22158104]
12. Karnani MM, et al. Opening holes in the blanket of inhibition: Localized lateral disinhibition by VIP interneurons. J Neurosci. 2016; 36:3471–3480. [PubMed: 27013676]
13. Donato F, Rompani SB, Caroni P. Parvalbumin-expressing basket-cell network plasticity induced by experience regulates adult learning. Nature. 2013; 504:272–6. [PubMed: 24336286]
14. Jiang X, Wang G, Lee AJ, Stornetta RL, Zhu JJ. The organization of two new cortical interneuronal circuits. Nat Neurosci. 2013; 162:210–218.
15. Pi HJ, et al. Cortical interneurons that specialize in disinhibitory control. Nature. 2013; 503:521–4. [PubMed: 24097352]
16. Fu Y, et al. A cortical circuit for gain control by behavioral state. Cell. 2014; 156:1139–1052. [PubMed: 24630718]
17. Zhou M, et al. Scaling down of balanced excitation and inhibition by active behavioral states in auditory cortex. Nat Neurosci. 2014; 17:841–50. [PubMed: 24747575]
18. Winer JA, Miller LM, Lee CC, Schreiner CE. Auditory thalamocortical transformation: structure and function. Trends Neurosci. 2005; 28:255–63. [PubMed: 15866200]
19. Smith PH, Uhlrich DJ, Manning KA, Banks MI. Thalamocortical projections to rat auditory cortex from the ventral and dorsal divisions of the medial geniculate nucleus. J Comp Neurol. 2012; 520:34–51. [PubMed: 21618239]
20. Ji XY, et al. Thalamocortical innervation pattern in mouse auditory and visual cortex: laminar and cell-type specificity. Cereb Cortex. 2016; 26:2612–25. [PubMed: 25979090]
21. Nahmani M, Erisir A. VGluT2 immunochemistry identifies thalamocortical terminals in layer 4 of adult and developing visual cortex. J Comp Neurol. 2005; 484:458–473. [PubMed: 15770654]
22. Rose HJ, Metherate R. Auditory thalamocortical transmission is reliable and temporally precise. J Neurophysiol. 2005; 94:2019–30. [PubMed: 15928054]
23. Cai D, Cohen KB, Luo T, Lichtman JW, Sanes JR. Improved tools for the Brainbow toolbox. Nat Methods. 2013; 10:540–7.
24. Marlin JJ, Carter AG. GABA-A Receptor inhibition of local calcium imaging in spines and dendrites. J Neurosci. 2014; 34:15898–911. [PubMed: 25429132]
25. Richardson RJ, Blundon JA, Bayazitov IT, Zakharenko SS. Connectivity patterns revealed by mapping of active inputs on dendrites of thalamorecipient neurons in the auditory cortex. J Neurosci. 2009; 29:6406–6417. [PubMed: 19458212]
26. Hackett TA, Barkat TR, O'Brien BMJ, Hensch TK, Polley DB. Linking topography to tonotopy in the mouse auditory thalamocortical circuit. J Neurosci. 2011; 31:2983–2995. [PubMed: 21414920]
27. Kanold PO, Nelken I, Polley DB. Local versus global scales of organization in auditory cortex. Trends Neurosci. 2014; 37:502–510. [PubMed: 25002236]
28. Stachniak TJ, Ghosh A, Sternson SM. Chemogenetic synaptic silencing of neural circuits localizes a hypothalamus pathway for feeding behavior. Neuron. 2014; 82:797–808. [PubMed: 24768300]
29. Kilgard MP, Merzenich MM. Cortical map reorganization enabled by nucleus basalis activity. Science. 1998; 279:1714–8. [PubMed: 9497289]
30. Froemke RC, Merzenich MM, Schreiner CE. A synaptic memory trace for cortical receptive field plasticity. Nature. 2007; 450:425–9. [PubMed: 18004384]
31. Miwa JM, et al. Lynx1, an endogenous toxin-like modulator of nicotinic acetylcholine receptors in the mammalian CNS. Neuron. 1999; 23:105–114. [PubMed: 10402197]

32. Morishita H, Miwa JM, Heintz N, Hensch TK. Lynx1, a cholinergic brake, limits plasticity in adult visual cortex. Science. 2010; 330:1238–1240. [PubMed: 21071629]
33. De Marco Garcia NV, Priya R, Tuncdemir SN, Fishell G, Karayannis T. Sensory inputs control the integration of neurogliaform interneurons into cortical circuits. Nat Neurosci. 2015; 18:393–401. [PubMed: 25664912]
34. Mesik L, et al. Functional response properties of VIP-expressing inhibitory neurons in mouse visual and auditory cortex. Front Neural Circuits. 2015; 9:22. [PubMed: 26106301]
35. Muralidhar S, Wang Y, Markram H. Synaptic and cellular organization of layer 1 of the developing rat somatosensory cortex. Front Neuroanat. 2014; 7:52. [PubMed: 24474905]
36. Knudsen EI. Capacity for plasticity in the adult owl auditory system expanded by juvenile experience. Science. 1998; 279:1531–1533. [PubMed: 9488651]
37. Hangya B, Ranade SP, Lorenc M, Kepecs A. Central cholinergic neurons are rapidly recruited by reinforcement feedback. Cell. 2015; 162:1155–68. [PubMed: 26317475]
38. Dahmen JC, Hartley DEH, King AJ. Stimulus-timing-dependent plasticity of cortical frequency representation. J Neurosci. 2008; 28:3629–13639.
39. Tasic B, et al. Adult mouse cortical cell taxonomy revealed by single cell transcriptomics. Nat Neurosci. 2016; 19:335–46. [PubMed: 26727548]
40. Batista-Brito R, et al. Developmental dysfunction of VIP interneurons impairs cortical circuits. Neuron. 2017; 95:884–895. [PubMed: 28817803]
41. Blundon JA, et al. Restoring auditory cortex plasticity in adult mice by restricting thalamic adenosine signaling. Science. 2017; 356:1352–1356. [PubMed: 28663494]
42. Bennett C, Arroyo S, Berns D, Hestrin S. Mechanisms generating dual-component nicotinic EPSCs in cortical interneurons. J Neurosci. 2012; 32:17287–96. [PubMed: 23197720]
43. Brown CE, Sweetnam D, Beange M, Nahirney PC, Nashmi R. α4* nicotinic acetylcholine receptors modulate experience-based cortical depression in the adult mouse somatosensory cortex. J Neurosci. 2012; 32:1207–1219. [PubMed: 22279206]
44. Yazaki-Sugiyama Y, Kang S, Cateau H, Fukai T, Hensch TK. Bidirectional plasticity in fast-spiking GABA circuits by visual experience. Nature. 2009; 462:218–21. [PubMed: 19907494]
45. Beurdeley M, et al. Otx2 binding to perineuronal nets persistently regulates plasticity in the mature visual cortex. J Neurosci. 2012; 32:9429–37. [PubMed: 22764251]
46. Engineer ND, et al. Reversing pathological neural activity using targeted plasticity. Nature. 2011; 470:101–4. [PubMed: 21228773]
47. Polley DB, Steinberg EE, Merzenich MM. Perceptual learning directs auditory cortical map reorganization through top-down influences. J Neurosci. 2006; 26:4970–4982. [PubMed: 16672673]
48. Fu Y, Kaneko M, Tang Y, Alvarez-Buylla A, Stryker MP. A cortical disinhibitory circuit for enhancing adult plasticity. Elife. 2015:e05558. [PubMed: 25626167]
49. Derégnaucourt S, Poirier C, Kant AV, Linden AV, Gahr M. Comparisons of different methods to train a young zebra finch (Taeniopygia guttata) to learn a song. J Physiol Paris. 2013; 107:210–8. [PubMed: 22982543]
50. Mowery TM, Kotak VC, Sanes DH. The onset of visual experience gates auditory cortex critical periods. Nat Commun. 2016; 7:10416. [PubMed: 26786281]
51. Hippenmeyer S, et al. A developmental switch in the response of DRG neurons to ETS transcription factor signaling. PLoS Biol. 2005; 3:e159. [PubMed: 15836427]
52. Taniguchi H, et al. A resource of cre driver lines for genetic targeting of GABAergic neurons in cerebral cortex. Neuron. 2011; 71:995–1013. [PubMed: 21943598]
53. Madisen L, et al. A toolbox of Cre-dependent optogenetic transgenic mice for light-induced activation and silencing. Nat Neurosci. 2012; 15:793–802. [PubMed: 22446880]
54. Madisen L, et al. Transgenic mice for intersectional targeting of neural sensors and effectors with high specificity and performance. Neuron. 2015; 85:942–58. [PubMed: 25741722]
55. Kobayashi A, et al. Lynx1 supports neuronal health in mouse dorsal striatum during aging: an ultrastructural investigation. J Mol Neurosci. 2014; 53:525–536. [PubMed: 25027556]

56. Meyer AH, Katona I, Blatow M, Rozov A, Monyer H. In vivo labeling of parvalbumin-positive interneurons and analysis of electrical coupling in identified neurons. J Neurosci. 2002; 22:7055–7064. [PubMed: 12177202]
57. Ichinohe N, Hyde J, Matsushita A, Ohta K, Rockland KS. Confocal mapping of cortical inputs onto identified pyramidal neurons. Front Biosci. 2008; 13:6354–73. [PubMed: 18508665]
58. Chattopadhyaya B, et al. Experience and activity-dependent maturation of perisomatic GABAergic innervation in primary visual cortex during a postnatal critical period. J Neurosci. 2004; 24:9598–9611. [PubMed: 15509747]
59. Takesian AE, Kotak VC, Sanes DH. Presynaptic $GABA_B$ receptors regulate experience-dependent development of inhibitory short-term plasticity. J of Neurosci. 2010; 30:2716–27. [PubMed: 20164356]
60. Alkondon M, Albuquerque EX. Diversity of nicotinic acetylcholine receptors in rat hippocampal neurons. I Pharmacological and functional evidence for distinct structural subtypes. J Pharmacol Exp Ther. 1993; 265:1455–73. [PubMed: 8510022]
61. Porter JT, et al. Selective excitation of subtypes of neocortical interneurons by nicotinic receptors. J Neurosci. 1999; 19:5228–35. [PubMed: 10377334]
62. Lucas-Meunier E, et al. Involvement of nicotinic and muscarinic receptors in the endogenous cholinergic modulation of the balance between excitation and inhibition in the young rat visual cortex. Cereb Cortex. 2009; 19:2411–27. [PubMed: 19176636]
63. Krause BM, Raz A, Uhlrich DJ, Smith PH, Banks MI. Spiking in auditory cortex following thalamic stimulation is dominated by cortical network activity. Front Syst Neurosci. 2014; 8:170. [PubMed: 25285071]
64. Saxena A, et al. Trehalose-enhanced isolation of neuronal sub-types from adult mouse brain. Biotechniques. 2012; 52:381–5. [PubMed: 22668417]
65. Livak KJ, Schmittgen TD. Analysis of relative gene expression data using real-time quantitative PCR and the 2(−Delta Delta C(T)) Method. Methods. 2001; 25:402–408. [PubMed: 11846609]
66. Cruikshank SJ, Rose HJ, Metherate R. Auditory thalamocortical synaptic transmission in vitro. J Neurophysiol. 2002; 87:361–384. [PubMed: 11784756]
67. Zhou X, Nagarajan N, Mossop BJ, Merzenich MM. Influences of unmodulated acoustic inputs on functional maturation and critical-period plasticity of the primary auditory cortex. Neuroscience. 2008; 154:390–396. [PubMed: 18304741]
68. Kim H, Bao S. Selective increase in representations of sounds repeated at an ethological rate. J Neurosci. 2009; 29:5163–5169. [PubMed: 19386912]
69. Geissler DB, Ehret G. Auditory perception vs. recognition: representation of complex communication sounds in the mouse auditory cortical fields. Eur J Neurosci. 2004; 19:1027–1040. [PubMed: 15009150]
70. Guo ZV, et al. Flow of cortical activity underlying a tactile decision in mice. Neuron. 2014; 81:179–94. [PubMed: 24361077]
71. Tsuriel S, Gudes S, Draft RW, Binshtok AM, Lichtman JW. Multispectral labeling technique to map many neighboring axonal projections in the same tissue. Nat Methods. 2015; 12:547–52. [PubMed: 25915122]

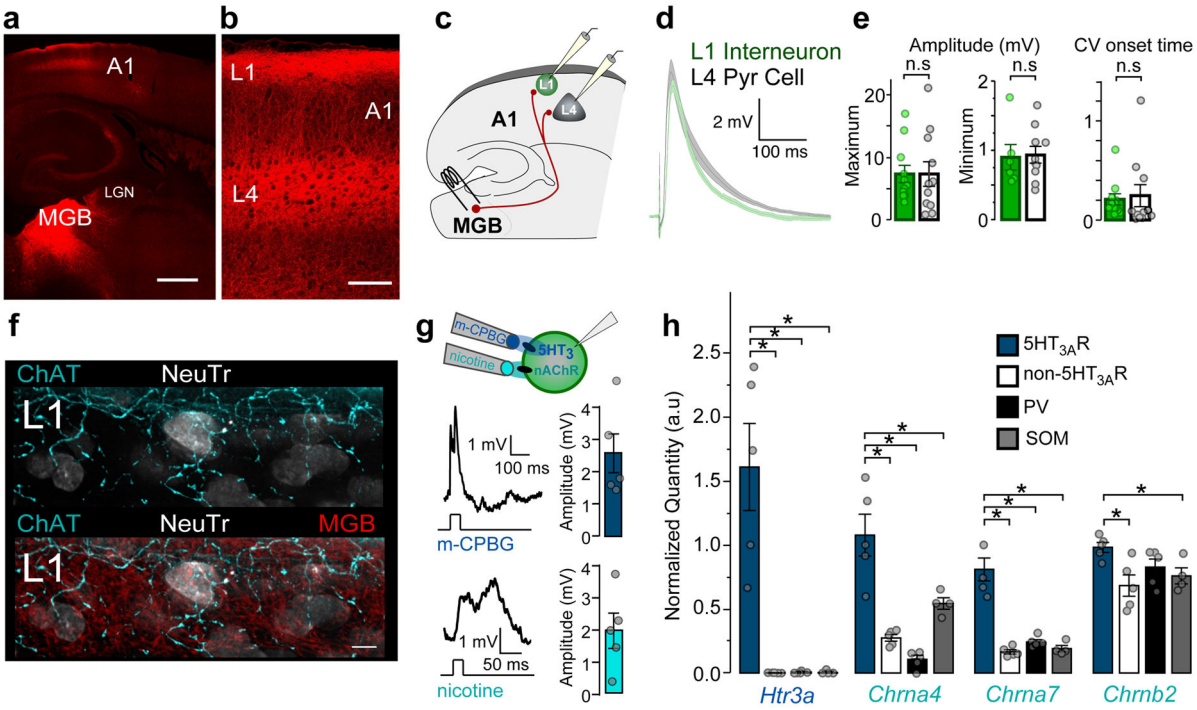

Figure 1. MGB and neuromodulatory inputs converge onto superficial 5-HT$_{3A}$R interneurons

(a,b) Projections from the medial geniculate body (MGB; red) to layers (L1) 1 and 4 of primary auditory cortex (A1). Scale bars = 500 μm, 100 μm. Representative image from one of 4 mice. (c) 5-HT$_{3A}$R cells receive direct MGB inputs. Schematic illustrating recording configuration. (d) Mean (± SEM, shaded region) EPSPs recorded in all L1 interneurons (green) and L4 pyramidal cells (gray) in response to electrical MGB fiber stimulation (L1, n = 11 cells/4 mice, L4, n = 11 cells/4 mice). (e) Left; Mean (± SEM) EPSP amplitudes evoked by maximal and minimal MGB fiber stimulation (EPSP maximum amplitude (mV): L1 = 6.91 ± 1.14, n = 11 cells/4 mice; L4 = 7.33 ± 1.96, n = 11 cells/4 mice; unpaired *t* test, two-tailed, t(20) = 0.19, P = 0.854; EPSP minimum amplitude (mV): L1 = 0.90 ± 0.18, n = 6 cells/4 mice; L4 = 0.94 ± 0.12, n = 10 cells/4 mice; Mann-Whitney *U* test, two-tailed, z = −0.27, P = 0.786). Right; Mean (± SEM) coefficient of variation (CV) of EPSP onset time (CV: L1 = 0.20 ± 0.06, n = 11 cells/4 mice; L4 = 0.25 ± 0.11, n = 11 cells/4 mice; Mann-Whitney *U* test, two-tailed z = −1.18, P = 0.237). (f) ChAT-expressing (cyan) and MGB axons (red) target L1 cells in A1 identified with Neurotrace (NeuTr, white). Scale bar = 5 μm. Representative image from one of 4 mice. (g) 5-HT$_{3A}$R interneurons are depolarized by ionotropic 5-HT$_3$ and nicotinic acetylcholine receptors (nAChRs). Left; Representative EPSPs evoked by focal application of nicotine or m-CPBG (100μM) recorded in 5-HT$_{3A}$R cells within L1 of A1. Right; Mean (± SEM) EPSP amplitudes (m-CPBG, 2.56 ± 0.64 mV, n = 5 cells/2 mice; nicotine, 1.99 ± 0.54 mV, n = 5 cells/2 mice). (h) Expression of *Htr3a*, *Chrna4*, *Chrna7*, and *Chrnb2* encoding 5-HT$_{3A}$R and nAChR subunits (α7, α4, and β2) measured within cortical interneuron subtypes using fluorescent-activated cell sorting (FACS) or A1 cells not expressing GFP after sorting 5-HT$_{3A}$R cells. (Normalized quantity *Htr3a*: 5-HT$_{3A}$R = 1.61 ± 0.34; non-5-HT$_{3A}$R = 0.002 ± 0.0007; PV = 0.005 ± 0.004; SST = 0.007 ± 0.007; Kruskal-Wallis, $\chi 2(3) = 11.29$, P = 0.010, compared to 5-HT$_{3A}$R using Steel

test, non-5-HT_{3A}R, P = 0.033; PV, P = 0.033; SST, P = 0.048; Normalized quantity *Chrna4*: 5-HT_{3A}R = 1.08 ± 0.16; non-5-HT_{3A}R = 0.27 ± 0.03; PV = 0.10 ± 0.03; SST = 0.54 ± 0.05; one-way ANOVA, F(3,15) = 22.95, P < 0.0001, compared to 5-HT_{3A}R using Dunnett's test, non-5-HT_{3A}R, P < 0.0001; PV, P < 0.0001; SST, P = 0.003; Normalized quantity *Chrna7*: 5-HT_{3A}R = 0.81 ± 0.09; non-5-HT_{3A}R = 0.17 ± 0.02; PV = 0.24 ± 0.02; SST = 0.19 ± 0.02; one-way ANOVA, F(3,15) = 38.98, P < 0.0001, compared to 5-HT_{3A}R using Dunnett's test, non-5-HT_{3A}R, P < 0.0001; PV, P < 0.0001; SST, P < 0.0001; Normalized quantity *Chrnb2*: 5-HT_{3A}R = 0.98 ± 0.04; non-5-HT_{3A}R = 0.68 ± 0.08; PV = 0.83 ± 0.06; SST = 0.76 ± 0.06; one-way ANOVA, F(3,15) = 4.01, P = 0.028, compared to 5-HT_{3A}R using Dunnett's test, non-5-HT_{3A}R, P = 0.012; PV, P = 0.238, SST, P = 0.081). n.s., P > 0.05, *P < 0.05.

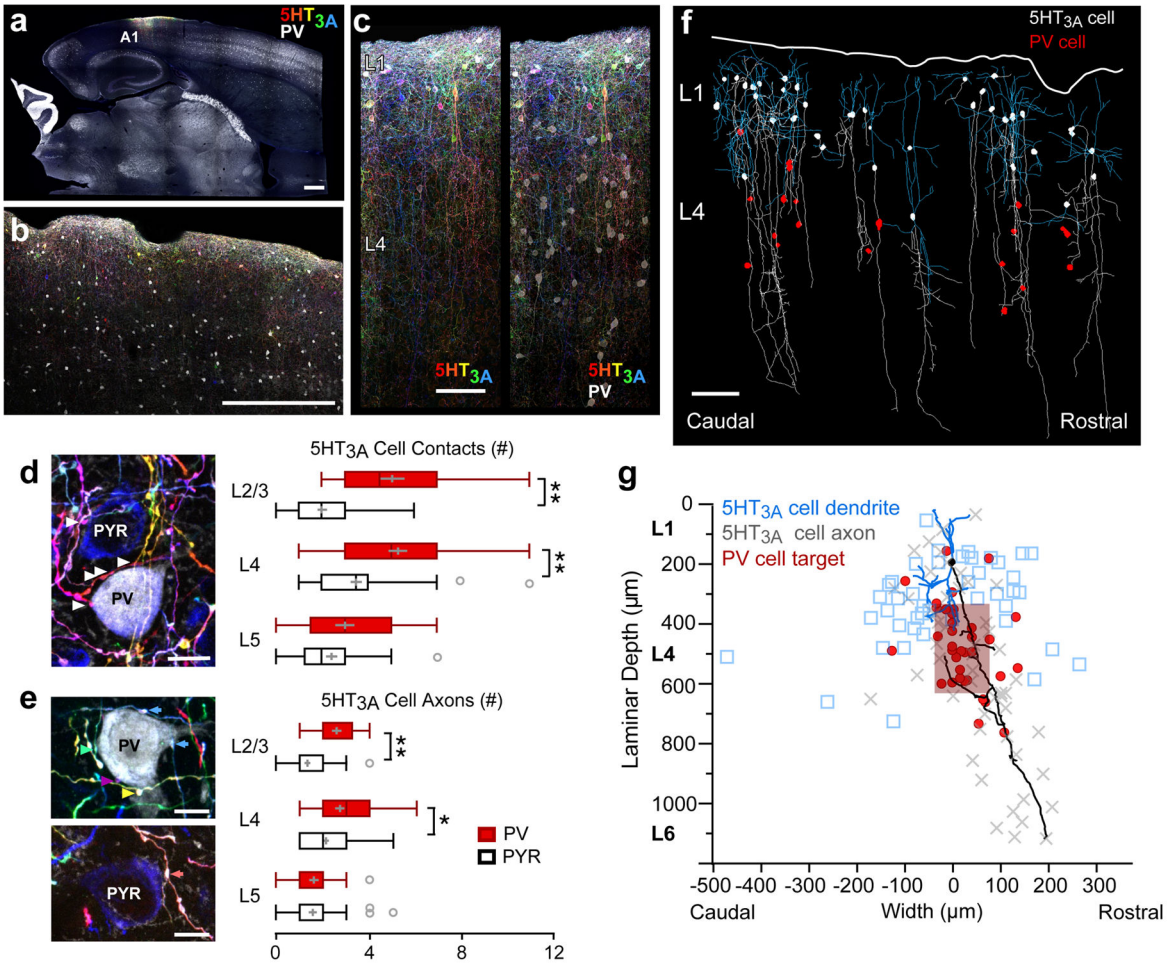

Figure 2. 5-HT$_{3A}$R interneurons target intracolumnar PV interneurons within L4

(a,b,c) Brainbow-expressing 5-HT$_{3A}$R and PV interneurons (white) in primary auditory cortex (A1) within a thalamocortical slice. Scale bars = 500 µm, 500 µm, 50 µm. Representative images from one of 4 mice. (d) Left; Brainbow-expressing 5-HT$_{3A}$R cell axons form numerous putative contacts onto a PV-expressing (white) cell soma, but only sparsely contact a pyramidal cell soma (PYR; blue) in L4 of A1. Representative image from one of 4 mice. Scale bar = 10 µm. Right; Number of 5-HT$_{3A}$R cell puncta forming putative contacts onto PV and pyramidal cell somata (L2/3: PV = 5.05 ± 0.54, n = 22 cells/4 mice; PYR = 2.00 ± 0.20, n = 53 cells/4 mice; unpaired *t* test, two-tailed, t(27) = −5.31, P < 0.001; L4: PV = 5.30 ± 0.40, n = 43 cells/4 mice; PYR = 3.50 ± 0.24, n = 62 cells/4 mice; unpaired *t* test, two-tailed, t(72) = −3.84, P = 0.0003; L5: PV = 3.00 ± 0.41, n = 21 cells/4 mice; PYR = 2.43 ± 0.24, n = 44 cells/4 mice; unpaired *t* test, two-tailed, t(63) = −1.25, P = 0.216). (e) More 5-HT$_{3A}$R cell axons target PV cell somata than pyramidal cell somata in cortical L2/3/4. Left; Unique Brainbow-expressing 5-HT$_{3A}$R-cell axons forming putative contacts (colored arrows) onto target cells can be distinguished by Brainbow-color. Representative image from one of 4 mice. Scale bars = 10 µm. Right; Number of 5-HT$_{3A}$R cell axons contacting PV and pyramidal cell somata (L2/3: PV = 2.59 ± 0.20, n = 22 cells/4 mice; PYR = 1.34 ± 0.12, n = 53 cells/4 mice; unpaired *t* test, two-tailed, t(73) = −5.39, P < 0.001; L4:

PV = 2.72 ± 0.20, n = 43 cells/4 mice; PYR = 2.13 ± 0.12, n = 62 cells/4 mice; unpaired *t* test, two-tailed, t(73) = −2.54, P = 0.013; L5: PV = 1.62 ± 0.20, n = 21 cells/4 mice; PYR = 1.57 ± 0.17, n = 44 cells/4 mice; unpaired *t* test, two-tailed, t(63) = −0.18, P = 0.858). Box plots show median, lower and upper quartiles (boxes), minima and maxima, and outliers (circles). Mean ± SEM shown in gray. (f) 5-HT_{3A}R-expressing cell axons (white) descend to contact PV cell somata (red) in L4 of A1. 5-HT_{3A}R cell dendrites are shown in blue. Representative image from one of 2 mice. Scale bar = 100 μm. (g) Maximal laminar depth and rostro-caudal width of all 5-HT_{3A}R cell (n = 54 cells/2 mice) dendrites (blue), axons (gray), and somatic innervation of PV cells (red; n = 36 cells/2 mice). Red box shows mean ± SD of PV cell innervation. Background illustrates representative reconstructed 5-HT_{3A}R cell soma (black), axon (black), and dendrites (blue). *P < 0.05, **P < 0.001.

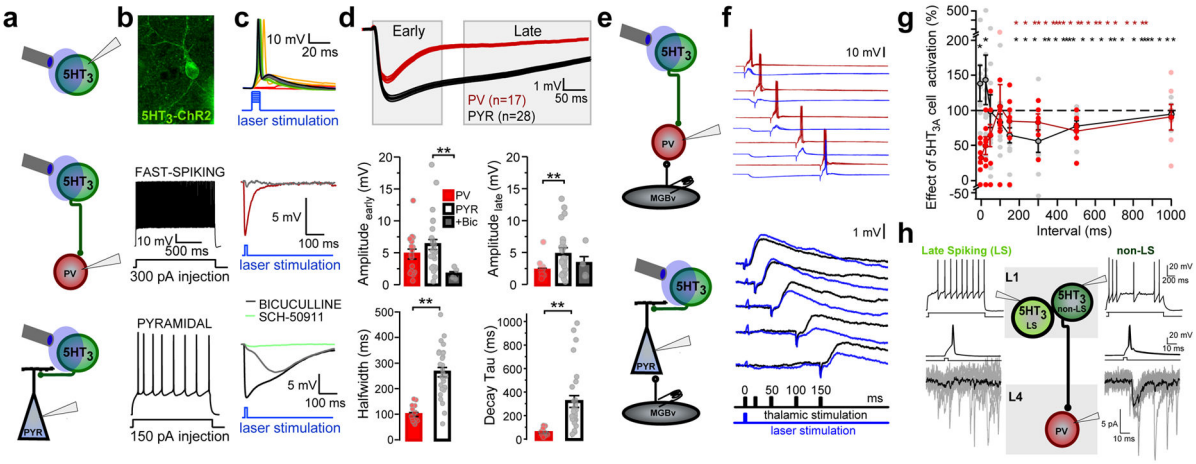

Figure 3. 5HT$_{3A}$R interneurons gate a window of disinhibition by differentially targeting PV and pyramidal cells

(a) Schematic of recording configurations. (b) 5HT$_{3A}$R-ChR2 expressing cell in L1 from A1 (top). Spiking responses to intracellular current injection in fast-spiking (middle) and pyramidal (bottom) cells. (c) Spiking responses of 5HT$_{3A}$R cell to increasing laser light (top; representative recording from one of 10 cells). 5HT$_{3A}$R cell-evoked IPSPs recorded in PV (middle; representative recording from one of 17 cells) and pyramidal cells (bottom; representative recording from one of 28 cells). IPSPs are shown in the presence of bath-applied bicuculline (5μM; gray; representative recording from one of 5 cells) and SCH-50911 (10μM; green; representative recording from one of 4 cells). (d) Top; Averaged (±SEM, shaded region) IPSPs recorded in all PV (red) and pyramidal cells (black). Middle; Mean (±SEM) peak amplitude of early (0–150 ms) and late (200–600 ms) IPSP components (early amplitude (mV): PV = 4.80 ± 0.77, n = 17 cells/12 mice; PYR = 6.29 ± 0.78, n = 28 cells/16 mice, BIC = 1.69 ± 0.38; n = 5 cells/4 mice; Kruskal-Wallis, $\chi 2(2) = 8.64$, P = 0.013, compared to PYR using Steel's test, PV, P = 0.470, BIC, P = 0.009; late amplitude (mV): PV = 1.98 ± 0.33; PYR = 4.84 ± 0.66; BIC = 3.02 ± 1.07; Kruskal-Wallis, $\chi 2(2) = 12.16$, P = 0.002, compared to PYR using Steel's test, PV, P = 0.001, BIC, P = 0.277). Bottom; Mean (±SEM) IPSP half-width and decay τ (IPSP half-width (ms): PV = 99.51 ± 7.65, n = 17 cells/12 mice; PYR = 264.33 ± 18.15, n = 28 cells/16 mice; unpaired *t* test, two-tailed, t(36) = 8.37, P < 0.0001; IPSP decay τ (ms): PV = 58.56 ± 7.02, n = 17 cells/12 mice; PYR = 321.34 ± 50.06, n = 28 cells/16 mice; Mann-Whitney *U* test, two-tailed, z = −4.74, P < 0.0001). (e) Schematic of recording configurations. Optogenetic activation of 5-HT$_{3A}$R cells followed by MGB electrical stimulation at varying intervals. (f) Top; Example PV cell recording shows that 5-HT$_{3A}$R cell activation suppresses MGB-evoked spiking responses. Bottom; Example pyramidal cell recording shows that 5-HT$_{3A}$R cell activation enhances MGB-evoked EPSPs for a brief time window before suppressing these responses. (g) Mean (± SEM) effects of 5-HT$_{3A}$R cell activation on spiking responses in PV cells (red) and EPSPs in pyramidal cells (black) at varying intervals between 5-HT$_{3A}$R cell activation and MGB stimulation (PV cell, n = 7 cells/5 mice; PYR cell, n = 12 cells/9 mice). (h) Single action potentials in a non-late-spiking (non-LS; right), but not LS (left), L1 interneuron produced reliable IPSCs in a PV interneuron in L4. (LS, recording from one of 2 paired connections; non-LS, recording from one of 8 paired connections). **P < 0.01.

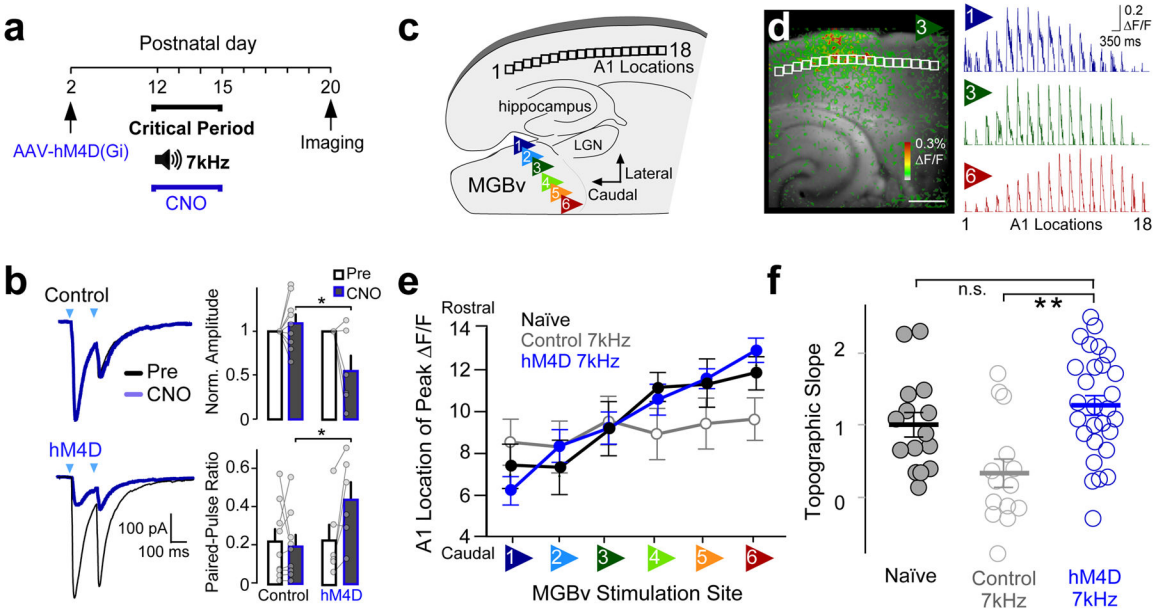

Figure 4. 5-HT$_{3A}$R cell silencing prevents tonotopic plasticity

(a) Timeline showing experimental strategy used to silence 5-HT$_{3A}$R cells during an auditory critical period. 5-HT$_{3A}$R-Cre mouse pups and littermate controls were injected with AAV-hSyn-DIO-hM4D(Gi)-mCherry, and administered CNO every 12hrs during sound exposure to pulsed 7kHz tone pips. Changes in thalamocortical connectivity were assessed using *in vitro* voltage-sensitive dye imaging (VSDI) at P20. (b) hM4D reduces 5-HT$_{3A}$R cell GABA release. Left; Representative 5-HT$_{3A}$R cell-evoked IPSCs recorded in L2/3 pyramidal cells in response to paired pulses of laser light (arrow) before (black trace) and following CNO bath application (15μM, blue trace) in slices from a P13 hM4D-expressing mouse and a littermate control. Right; Mean (± SEM) normalized amplitudes (control = 1.09 ± 0.10, n = 9 cells/2 mice; hM4d = 0.55 ± 0.18, n = 6 cells/3 mice; unpaired *t* test, two-tailed, t(13) = −2.89, P = 0.013) and paired-pulse ratio (PPR: control = 0.19 ± 0.06, n = 9 cells/2 mice; hM4d = 0.44 ± 0.09, n = 6 cells/3 mice; unpaired *t* test, t(13) = 2.40, P = 0.032, inter-stimulus-interval = 80). (c) Schematic of an auditory thalamocortical slice illustrates the six stimulus positions within the ventral medial geniculate body (MGBv) and locations analyzed within L4 of the primary auditory cortex (A1). (d) Left; Example of A1 responses (ΔF/F) to stimulation of MGBv position 3 using VSDI. Scale bar = 500 μm. Right; Average normalized traces (ΔF/F) across A1 locations to stimulation of MGBv positions 1, 3, and 6 (n = 28 mice). (e) Mean (± SEM) location of cortical L4 peak ΔF/F to MGBv stimulations (Naïve, n = 15 mice; Control 7kHz, n = 14 mice; hM4D 7kHz, n = 28 mice). (f) Mean (± SEM) topographic slopes (C57 Naïve = 1.01 ± 0.17, n = 15 mice; control 7kHz, 0.34 ± 0.20, n = 14 mice; hM4d 7kHz, 1.27 ± 0.14, n = 28 mice; one-way ANOVA, F(2,54) = 8.20, P = 0.0008, compared to hM4d 7kHz using Dunnett's test, C57 Naïve, P = 0.41, control, P = 0.0003). n.s., P > 0.05, *P < 0.05, **P < 0.001.

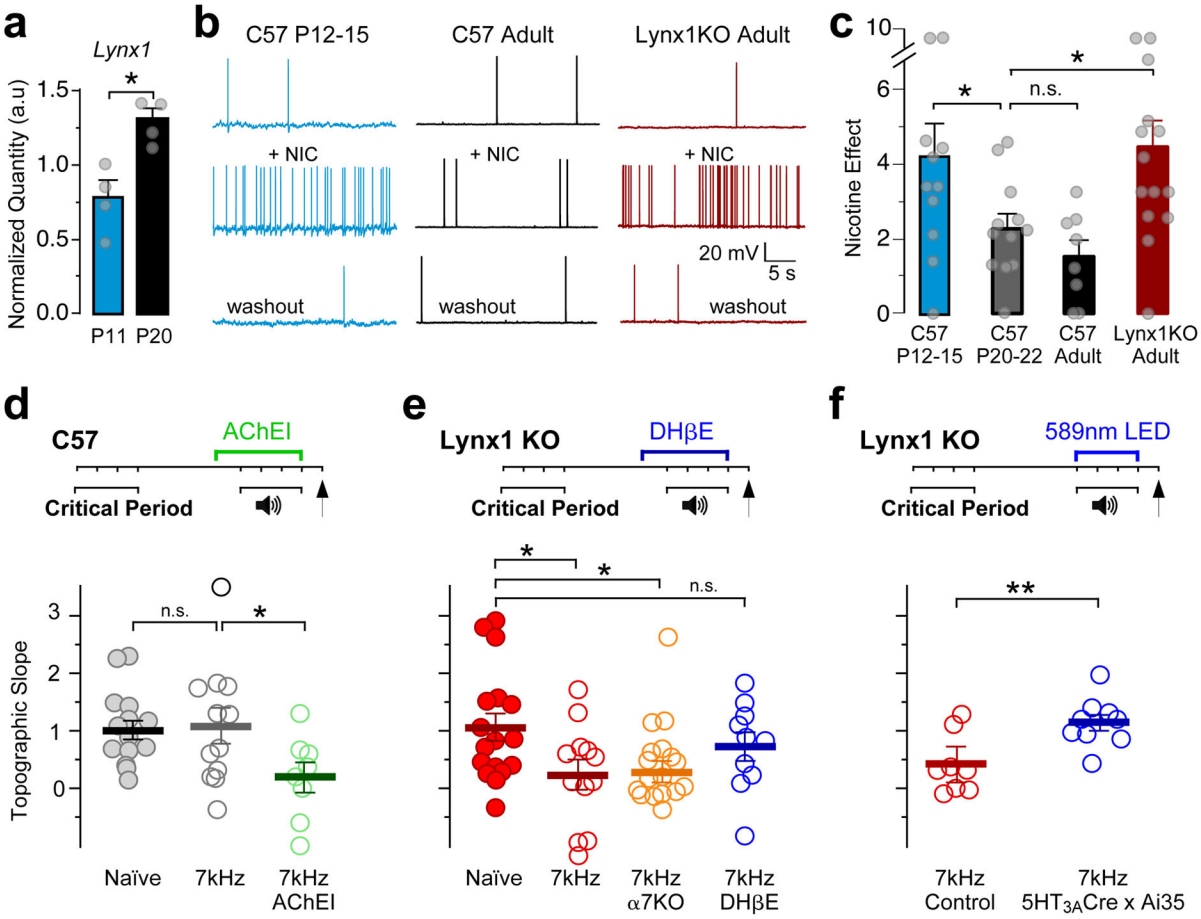

Figure 5. Nicotinic recruitment of 5-HT$_{3A}$R cells controls critical period timing

(a) *Lynx1* expression within 5-HT$_{3A}$R cells increases between postnatal day (P) 11 and 20 (normalized *Lynx1* quantity: P11 = 0.77 ± 0.11; P20 = 1.30 ± 0.07, n = 4 mice each; Mann-Whitney *U* test, two-tailed, z = 2.17, P = 0.030). (b) Representative 5-HT$_{3A}$R cell spiking responses before (top), during nicotine application (middle; bath-applied; 10μM), and following 15m washout (bottom). (c) Mean (± SEM) nicotine effect on spiking responses (C57 P12–15 = 4.18 ± 0.93, n = 11 cells/5 mice; C57 P20–22 = 2.28 ± 0.38, n = 12 cells/5 mice; C57 adult = 1.52 ± 0.43, n = 8 cells/8 mice; Lynx1 KO adult = 4.44 ± 0.74, n = 14 cells/10 mice; Kruskal-Wallis, $\chi 2(2) = 12.55$, P = 0.0057, compared to C57 adult using Steel Test, C57 P12–15, P = 0.046, C57 P20–22, P = 0.56, Lynx1 KO, P = 0.013). (d–f) Top; Timelines showing experimental strategies. Bottom; Mean (± SEM) topographic slopes (d, Naïve = 1.01 ± 0.17, n = 15 mice; 7kHz = 1.09 ± 0.30, n = 12 mice; 7kHz AChEI = 0.19 ± 0.26, n = 8 mice; one-way ANOVA, F(2,32) = 3.30, P = 0.049, compared to 7kHz using Dunnett's test, Naïve, P = 0.96, 7kHz AChEI, P = 0.044; e, Naïve = 1.05 ± 0.24, n = 17 mice; 7kHz = 0.23 ± 0.26, n = 12 mice, 7kHz α7 KO = 0.28 ± 0.19, n = 19 mice, 7kHz DHβE = 0.73 ± 0.25, n = 10 mice; one-way ANOVA, F(3,54) = 3.09, P = 0.035, compared to Naïve with Dunnett's test, 7kHz, P = 0.044, 7kHz α7 KO, P = 0.031, 7kHz DHβE, P = 0.69; f, 7kHz control = 0.41 ± 0.18, n = 8 mice; 7kHz 5-HT$_{3A}$-Cre x Ai35 = 1.14 ± 0.14, n =

9 mice; unpaired *t* test, two-tailed, t(15) = −3.20, P = 0.006). n.s., P > 0.05, *P < 0.05, **P < 0.01.

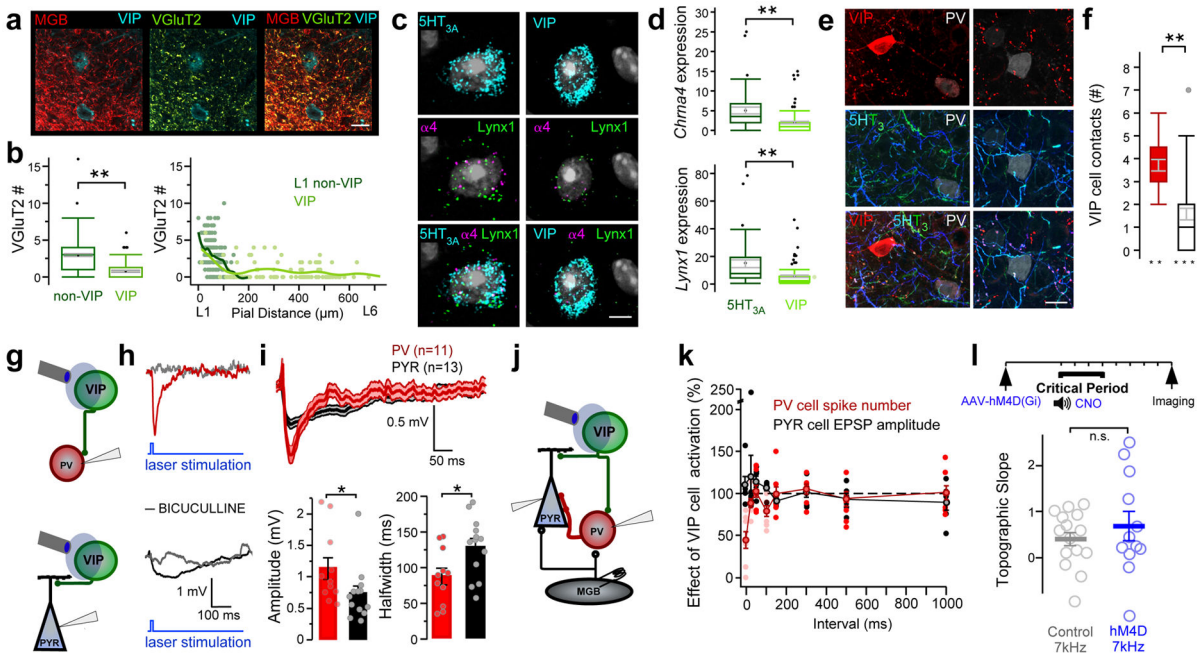

Figure 6. VIP cells contribute to PV cell suppression, but are not necessary for CP plasticity

(a) MGB puncta (red) onto VIP-expressing interneurons in L1 colocalize with vGluT2 (green). Scale bar = 5μm. Representative image from one of 3 mice. (b) Left; VIP cells receive less vGluT2 puncta compared to L1 non-VIP cells (number of vGluT2 puncta: non-VIP = 2.96 ± 0.17, n = 190 cells/3 mice; VIP = 0.77 ± 0.13, n = 98 cells/3 mice; Mann-Whitney *U* test, two-tailed, z = −8.45, P < 0.0001). Box plots show median, lower and upper quartiles (boxes), minima and maxima, and outliers (circles). Mean ± SEM shown in gray. Right; Number of vGluT2 puncta onto L1 non-VIP and VIP cells across cortical lamina. (c) VIP interneurons express less mRNA encoding α4 nAChR subunits and Lynx1 than the general 5-HT_{3A}R cell population. *In situ hybridization* shows colocalization of *Chrna4* and *Lynx1* mRNAs encoding α4 nAChR subunits and Lynx1 in *Htr3a* (5-HT_{3A}R) and *VIP* (VIP)-expressing cells. Scale bar = 5 μm. (d) Quantification of detected *Chrna4* and *Lynx1* mRNA copies per 5-HT_{3A}R or VIP cell (*Chrna4*: 5-HT_{3A}R = 5.08 ± 0.87, n = 40 cells/3 mice; VIP = 2.01 ± 0.31, n = 96 cells/3 mice; Mann-Whitney *U* test, two-tailed, z = 4.91, P < 0.0001; *Lynx1*: 5-HT_{3A}R = 14.68 ± 2.81, n = 40 cells/3 mice; VIP = 5.08 ± 0.82, n = 96 cells/3 mice; Mann-Whitney *U* test, two-tailed, z = 4.62, P < 0.0001). Box plots show median, lower and upper quartiles (boxes), minima and maxima, and outliers (circles). Mean ± SEM shown in gray. (e) Representative 5-HT_{3A}R cell axons (blue/green) expressing VIP (red) form putative contacts onto L4 PV-expressing cell somata (white). (f) VIP-expressing interneurons form numerous putative contacts onto PV cell somata, but only sparsely contact pyramidal (PYR) cell somata in L4 of A1 (number of VIP cell puncta: PV = 3.71 ± 0.25, n = 21 cells; PYR = 1.58 ± 0.25, n = 40 cells; from 3 mice; Mann-Whitney *U* test, two-tailed, z = 4.77, P < 0.0001). Box plots show median, lower and upper quartiles (boxes), minima and maxima, and outliers (circles). Mean ± SEM shown in gray. (g) Schematic of recording configurations. (h) VIP cell-evoked IPSPs recorded in PV cell (top) and pyramidal cell (bottom) within L4. IPSPs are shown in the presence of bath-applied bicuculline (5μM; gray; examples from one each of 3 PV cells and 3 pyramidal cells). (i) Top; Averaged (±SEM,

shaded region) IPSPs recorded in all PV (red) and pyramidal cells (black). Bottom; Mean (±SEM) peak IPSP amplitude and half-width (IPSP amplitude (mV): PV = 1.13 ± 0.17, n = 11 cells/5 mice; PYR = 0.73 ± 0.12, n = 13 cells/6 mice; Mann-Whitney *U* test, two-tailed, z = 2.14, P = 0.032; half-width (ms): PV = 87.44 ± 11.68, n = 11 cells/5 mice; PYR = 129.43 ± 11.50, n = 13 cells/6 mice; unpaired *t* test, two-tailed, t(22) = 2.56, P = 0.018). (j) Schematic of recording configurations. (k) Mean (± SEM) effects of VIP cell activation on spiking responses in PV cells (red) and EPSPs in pyramidal cells (black) at varying intervals between VIP cell activation and MGB stimulation (PV cell, n = 8 cells/5 mice; PYR cell, n = 6 cells/6 mice). (l) VIP cell silencing does not disrupt tonotopic plasticity. Top; Timeline showing experimental strategy. Bottom; Mean (± SEM) topographic slopes (control 7kHz = 0.41 ± 0.15, n = 16 mice; hM4d 7kHz = 0.70 ± 0.32, n = 12 mice; unpaired *t* test, two-tailed, t(16) = 0.83, P = 0.42). n.s., P > 0.05, *P < 0.05, **P < 0.0001.

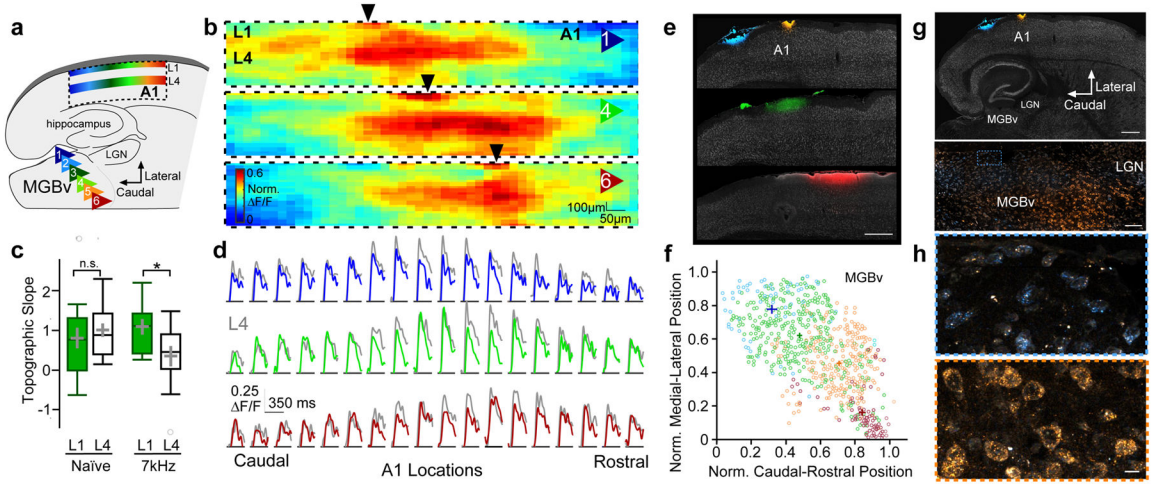

Figure 7. A cortical L1 map tunes auditory cortex

(a) Schematic illustrating a topographic map of MGBv inputs to cortical L1 that mirrors L4. (b) Mean peak responses (norm. ΔF/F) across A1 to stimulation of MGBv positions 1, 4, and 6 across all animals using VSDI (n = 15 mice). Black arrows indicate the rostro-caudal location of peak responses within L1. (c) Topographic slopes within L1 and L4 of naïve mice and those exposed to 7kHz during the critical period (Naïve: L1 = 0.81 ± 0.26, n = 15 mice; L4 = 1.01 ± 0.17, n = 15 mice; unpaired *t* test, two-tailed, t(28) = 0.642, P = 0.526; 7kHz: L1 = 1.09 ± 0.20, n = 11 mice; L4 = 0.35 ± 0.26, n = 11 mice; unpaired *t* test, two-tailed, t(20) = −2.29, P = 0.033). Box plots show median, lower and upper quartiles (boxes), minima and maxima, and outliers (circles). Mean ± SEM shown in gray. (d) Average normalized traces (ΔF/F) across A1 locations (n = 15 mice) to stimulation of MGBv positions 1, 4, and 6 in L1 (colored) and L4 (gray). (e) Topographic projections from MGBv to L1. Focal injections of fluorescent dyes conjugated to wheat germ agglutinin (WGA) along the rostral-caudal axis within L1 of A1 from 3 mice. Scale bar = 500 μm (f) Scatter plot showing normalized position of all MGBv cells containing dye-labeled vesicles from 4 injections in 3 mice (colors indicate injections shown in e). Crosses show mean (± SEM) caudal-rostral and medial-lateral positions. (g) Thalamocortical slice of mouse injected with WGA in rostral and caudal sites within L1 of A1. Scale bars = 500 μm, 100 μm. (h) Dye-labeled vesicles in caudolateral (top; blue) and rostromedial (bottom; orange) MGBv locations from caudal and rostral A1 injections, respectively. Scale bar = 10 μm. n.s., P > 0.05, *P < 0.05.